
DiTTO: DIFFUSION-INSPIRED TEMPORAL TRANSFORMER OPERATOR

Oded Ovadia, Eli Turkel

Department of Applied Mathematics
Tel Aviv University
Tel Aviv

odedovadia@mail.tau.ac.il, eliturkel@gmail.com

Adar Kahana, George Em Karniadakis

Division of Applied Mathematics
Brown University
Providence, RI

adar_kahana@brown.edu, george_karniadakis@brown.edu

ABSTRACT

Solving partial differential equations (PDEs) using a data-driven approach has become increasingly common. The recent development of the operator learning paradigm has enabled the solution of a broader range of PDE-related problems. We propose an operator learning method to solve time-dependent PDEs continuously in time without needing any temporal discretization. The proposed approach, named DiTTO, is inspired by latent diffusion models. While diffusion models are usually used in generative artificial intelligence tasks, their time-conditioning mechanism is extremely useful for PDEs. The diffusion-inspired framework is combined with elements from the Transformer architecture to improve its capabilities.

We demonstrate the effectiveness of the new approach on a wide variety of PDEs in multiple dimensions, namely the 1-D Burgers' equation, 2-D Navier-Stokes equations, and the acoustic wave equation in 2-D and 3-D. DiTTO achieves state-of-the-art results in terms of accuracy for these problems. We also present a method to improve the performance of DiTTO by using fast sampling concepts from diffusion models. Finally, we show that DiTTO can accurately perform zero-shot super-resolution in time.

Keywords Scientific machine learning · Diffusion models · Transformers · Partial differential equations

1 Introduction

The field of scientific machine learning (SciML) has been growing rapidly in recent years, successfully modeling [1, 2, 3] and discovering [4, 5] scientific problems and applications using machine learning (ML) methods. This is a result of the significant advances in the field of ML, with state-of-the-art methods being developed daily. Appropriately used, many tools designed for standard ML and data science problems can also perform well on SciML tasks. These ML methods come from various domains, such as natural language processing, image classification, time-series analysis, etc. This work aims to use elements from a recently proposed method called *diffusion models* and adapt them for solving forward partial differential equations (PDEs).

Solving PDEs is an essential topic for the scientific community. This centuries-old research involves formulating a problem from physical domains, biological research, chemical reactions, etc., and using numerical tools to evaluate or approximate the phenomena. Therefore, the applications of this research area can be found in many fields, such as acoustic wave propagation [6, 7], computational mechanics [8, 9], fluid dynamics [10, 11], seismic imaging [12],

and so on. However, as the problems become more complex, the difficulty in solving them using classical numerical methods is greater. Consequently, SciML methods are often helpful in such scenarios.

There are two main types of PDE-related problems: forward and inverse problems. Forward problems focus on solving or approximating the solution of a physical process from a certain point in time to a later point. Inverse problems discuss using measurements of the solution to recover information about the problem itself. While many SciML methods were shown to be valid for inverse problems [1, 3, 13], the focus of this work is forward problems. When using computer simulations, one usually cannot compute the exact solution, as the problem is continuous, but the simulation is discrete. Therefore, a simulation is created to find an approximate solution. In this case, there exists a trade-off between the computational demands and the accuracy of the method, which is directly influenced by the spatial and temporal discretization of the problem. Finding an accurate continuous numerical solution for a forward problem is challenging and is the main focus of this work.

Solving PDE-related problems involves several challenges. Two such challenges are generalizations for different problem conditions and dependency on the physical domain’s discretization. Tackling the first, we utilize tools from the growing field of operator learning, where we attempt to use learning techniques to map a function space to another one. Thus, we are able to learn a family of solutions of PDEs corresponding to a family of initial conditions. For the latter challenge, we develop a method that is meshfree in time. While it is dependent on the spatial discretization, the temporal aspect of the solution, which is a prominent challenge for solvers of dynamical systems, is continuous.

The structure of this paper is as follows. In Section 2, we give an overview of key components of the proposed method, such as operator learning, diffusion models, and transformers. In Section 3, we describe the proposed method and its architecture in detail. In Section 4, we demonstrate the effectiveness of the proposed method on a number of different datasets. Finally, in Appendix A, we show additional results and experiments.

2 Background and related work

2.1 Operator learning

The standard use of ML models for scientific computations involves fitting a function to map numerical inputs to outputs. These inputs are ordinarily coordinates, materials, boundary conditions, etc., and the outputs are usually solutions of forward PDEs. An example is physics-informed neural networks (PINNs) [1], which use a deep neural network to solve PDEs by embedding elements from the PDE problem into the loss function. In this way, the network trains on the given data while using prior information about the problem it is solving. One major drawback is that for each problem, one needs to re-train the network, which is computationally expensive. This includes any changes to the parameters defining the problem, such as the inputs mentioned above.

The growing field of operator learning seeks to overcome this problem. Instead of fitting a function, one attempts to fit a mapping between two families of functions. Mathematically, let us consider a generic family of d -dimensional time-dependent PDE problems of the form:

$$\begin{cases} \mathcal{L}u(\mathbf{x}, t) = f(\mathbf{x}, t), & \mathbf{x} \in D, t \in [0, t_{final}] \\ \mathcal{B}u(\mathbf{x}, t) = g(\mathbf{x}, t), & \mathbf{x} \in \partial D, t \in [0, t_{final}] \\ u(\mathbf{x}, 0) = I(\mathbf{x}), & \mathbf{x} \in D \end{cases}, \quad (1)$$

where the differential operator \mathcal{L} and forcing term f define the PDE, the boundary operator \mathcal{B} and boundary condition g define the solution on the boundary, t_{final} is the final physical time, I is the initial condition, and D is a Euclidean domain in \mathbb{R}^d with boundary ∂D . We assume that the problem (1) is well-posed [14], so a unique solution exists.

Let \mathcal{I} be a function space containing initial conditions of (1). Then there exists another space \mathcal{U} that contains their respective solutions. We can define an operator $\mathcal{G} : \mathcal{I} \rightarrow \mathcal{U}$ as follows:

$$\mathcal{G}(I)(\mathbf{x}, t) = u(\mathbf{x}, t), \quad (2)$$

where $I \in \mathcal{I}$, $\mathbf{x} \in D$, and $t \in [0, t_{final}]$. So, each initial condition $I \in \mathcal{I}$ is mapped into its corresponding solution $u \in \mathcal{U}$. The goal is to approximate the operator \mathcal{G} using a neural network.

The first SciML operator learning method, called DeepONet, was proposed by Lu et al. [2]. The main components of a DeepONet are two neural networks: the branch and the trunk. Each network can be a fully-connected neural network, convolutional, or any other architecture. Usually, the branch inputs are functions, and the trunk inputs are coordinates.

The DeepONet learns projections from the functions to a vector space, so it can map input functions to output functions at specific points.

Another operator learning approach is the Fourier neural operator (FNO) [3, 15]. FNOs, similarly to DeepONets, learn mappings between function spaces using projections. Specifically, FNOs utilize the Fourier transform. They are effective and easy to implement, gaining traction in the SciML community. FNOs are accurate, especially for smooth and periodic problems [16]. We note that while the Fourier kernel is continuous, it is necessary to use discrete versions for operator learning in practice. Consequently, FNOs can be computationally costly when working with high-dimensional problems requiring many Fourier modes.

2.2 Transformers and attention

First presented by Vaswani et al. [17], transformers have been widely used in the ML community. Transformers introduce a new type of mechanism called the *scaled dot-product attention*. The attention module attempts to gather context from the given input. It does so by operating on a discrete embedding of the data composed of discrete tokens.

The original architecture was proposed for natural language processing purposes, where one can encode sentences using their enumerated locations in the vocabulary. Since then, their usage has been extended to many other domains, and they outperform many different deep learning architectures in a wide variety of tasks. These domains include time series analysis [18] and computer vision [19]. For example, Vision Transformers (ViT) [20] split images into small patches, tokenize them, and apply the attention mechanism. In addition, they are significantly lighter than other alternatives and can be easily parallelized.

Transformers are becoming increasingly popular across the SciML community as well. Transformers have been used for operator learning in many different ways [21, 22, 23, 24]. These methods show much promise by using the attention mechanism to find connections between points in the physical domain to function values. Some methods emphasize the attention mechanism itself [25, 26] and adapt it to PDE-related problems. Others utilize existing transformer models to help the SciML community solve problems more easily [27]. In this work, we employ elements from the original Transformer architecture as part of the proposed neural network architecture.

2.3 Diffusion models

A diffusion model is a generative deep learning model that uses a Markov chain to produce samples that match a given dataset [28]. These models essentially aim to learn the underlying distribution of a given dataset. After learning this distribution, they are used to generate new samples of similar properties to those found in the training set.

In [29], Ho et al. introduced a new type of diffusion model called denoising diffusion probabilistic models (DDPM). It consists of a forward diffusion process and an inverse one. In the forward case, Gaussian noise is incrementally added to the original sample for a given number of iterations. For a sufficiently large number of iterations, the noise completely destroys the original signal. Then, in the reverse diffusion process, the goal is to reconstruct the original signal by performing iterative denoising steps using a neural network. Diffusion models have been used for SciML purposes, especially for generative artificial intelligence purposes [30, 31, 32]. While we are not using their generative capabilities in this work, we briefly explain their standard training procedure.

We present a mathematical formulation mostly based on the works of Ho et al. [29] and Nichol et al. [33]. Given a data distribution $x_0 \sim q(x_0)$, we define a forward noising process q which produces steps x_1, \dots, x_T by adding Gaussian noise at time t with variance $\beta_t \in (0, 1)$ as follows:

$$q(x_1, \dots, x_T | x_0) := \prod_{t=1}^T q(x_t | x_{t-1}), \quad (3)$$

$$q(x_t | x_{t-1}) := \mathcal{N}(x_t; \sqrt{1 - \beta_t} x_{t-1}, \beta_t \mathbf{I}). \quad (4)$$

Given a sufficiently large T and a well-behaved schedule β_t , the latent x_T is nearly an isotropic Gaussian distribution. From (4), we see that x_t is drawn from a conditional Gaussian distribution with mean $\mu_t = \sqrt{1 - \beta_t} x_{t-1}$ and variance $\sigma_t^2 = \beta_t$. In practice, this is done by randomly sampling a noise level parameter $\varepsilon \sim \mathcal{N}(\mathbf{0}, \mathbf{I})$, and setting:

$$x_t = \sqrt{1 - \beta_t} x_{t-1} + \sqrt{\beta_t} \varepsilon. \quad (5)$$

Thus, if we know the exact reverse distribution $q(x_{t-1}|x_t)$, we can sample $x_T \sim \mathcal{N}(0, \mathbf{I})$ and run the process in reverse to get a sample from $q(x_0)$. However, since $q(x_{t-1}|x_t)$ depends on the entire data distribution, we approximate it using a neural network with hyperparameters θ as follows:

$$p_\theta(x_{t-1}|x_t) := \mathcal{N}(x_{t-1}; \mu_\theta(x_t, t), \Sigma_\theta(x_t, t)). \quad (6)$$

The neural network needs to learn the mean and variance to complete the backward diffusion process. Importantly for this case, using the formulation in (5), in each step, it is sufficient to know β_t, x_t , and ε to approximate x_{t-1} . Then, the network is used autoregressively to reconstruct x_0 . Assuming we know the schedules $\{\beta_t\}_{t=1}^T$ beforehand, we can view the neural network as the following mapping:

$$(x_t, \varepsilon) \longrightarrow x_{t-1}. \quad (7)$$

In each step, the neural network performs a denoising operation, mapping x_t to a slightly less noisy signal x_{t-1} . Including the noise level parameter ε is essential for the denoising operation. During training, various noise levels are sampled, and knowing the specific noise level that distinguishes between consecutive states x_t and x_{t-1} , is crucial for effective denoising. Without this explicit knowledge of the noise level, the denoising process would become significantly more complicated, and the network may not converge. This means we have a conditional denoising operation, conditioned on ε (or equivalently on the timestep with β_t).

3 Methodology

3.1 Diffusion-inspired operator learning

We combine the formulations in Section 2.1 and Section 2.3 to define a new data-driven approach for operator learning. In this approach, the time evolution of the PDE solution is viewed as a forward process. Instead of incrementally adding noise to the inputs, we incrementally evolve the PDE solution over time. We replace the noise level parameter ε with the temporal variable t . Then, we use the conditioning capabilities of diffusion models to learn the relations between the initial condition, the PDE solution, and the time domain. After training is complete, the model can interpolate between the initial and final time, creating a numerical solution that is continuous in time.

Mathematically, given a PDE solution u , we define a continuous forward process:

$$\{x_t | t \in [0, t_{final}], x_t := u(\mathbf{x}, t)\}, \quad (8)$$

where x_t is the initial condition for $t = 0$, and for $t = t_{final}$, x_t is the solution at the final time. To agree with the notations commonly used in the ML community, we use x to mark a sample or data point. To avoid confusion, the spatial element \mathbf{x} is not necessarily related to the data point x . Using this notation, the operator learning problem (2) becomes:

$$x_0 \longrightarrow x_t, \forall t \in [0, t_{final}]. \quad (9)$$

We further observe that while this formulation is inspired by diffusion models, it differs from the diffusion process described in Section 2.3 in many aspects. Most importantly, we do not view x_0, x_1, \dots, x_T as an iterative process. Rather, the goal is to directly approximate $u(\mathbf{x}, t)$ continuously without any prior information on the temporal evolution of the solution. Using similar notations to Section 2.3, the ultimate goal is to estimate $p_\theta(x_t|x_0)$ using a neural network, and not $p_\theta(x_t|x_{t-1})$. We also note that this process is not necessarily a Markovian process. Moreover, we are not interested in a reverse process since we are solving a forward problem.

The diffusion process discussed in Section 2.3 is discrete, while (8) is continuous. We discretize $\{x_t\}$ by taking a partitioning $\{t_n\}_{n=0}^T$ of $[0, t_{final}]$, where $0 = t_0 < t_1 < \dots < t_{T-1} < t_T = t_{final}$. The discrete process is then defined as $\{x_n\}_{n=0}^T$, where $x_n := u(\mathbf{x}, t_n)$. Then, the discrete operator learning problem is given by:

$$x_0 \longrightarrow x_n, n = 1, \dots, T. \quad (10)$$

In PDE terms, given an initial condition x_0 , we approximate the analytic solution at a set of specific future time steps $\{t_n\}_{n=1}^T$. In operator learning terms, we map a family of functions of the form $x_0 = u(\mathbf{x}, 0)$ to another family of functions of the form $u(\mathbf{x}, t)$.

As outlined before, the role of the neural network in diffusion models is to perform conditional denoising in each step. We repurpose this exact network structure to solve a PDE-related problem. Since x_0, x_1, \dots, x_T are directly taken from the analytical solution, we have no noise in this process. Therefore, there is no need for denoising. Thus, we replace the conditional denoising operation with a conditional temporal evolution. Mathematically, the mapping (10) becomes:

$$(x_0, t_n) \longrightarrow x_n. \quad (11)$$

So, each sample the neural network encounters during the training stage is composed of three elements: an initial condition x_0 , a desired time t_n , and the analytic solution corresponding to x_0 at time t_n , i.e., $x_n = u(\mathbf{x}, t_n)$. At inference, only an initial condition and a desired time are given, and the network infers the solution at the desired time.

We point out that even though the described process does not have any noise or other perturbations, from an application point of view, it is possible to include noise in various ways to create a more realistic scenario. To better understand the approach, we present the generic formulation without addressing noise.

3.2 Training dataset

To train a neural network using the formulation presented in Section 3.1, we require a large set of initial conditions (inputs) and corresponding solutions (outputs). Let $\{I^m(\mathbf{x})\}_{m=1}^M$ be a set of initial conditions with corresponding analytic solutions $\{u^m(\mathbf{x}, t)\}_{m=1}^M$, where M is the desired number of training samples. Each sample consists of an initial condition and a PDE solution at the relevant timesteps. We note that in practice, $\{u^m(\mathbf{x}, t)\}_{m=1}^M$ are accurate numerical approximations of the analytic solutions and not analytic solutions which are often unavailable. Furthermore, the solutions are discretized in space using a grid that partitions the domain D . We emphasize that for all $m = 1, \dots, M$ and $t = 0, \dots, T$, $u^m(\mathbf{x}, t)$ is a matrix, and its dimensions depend on the spatial discretization parameters, i.e., the number of nodes along each axis.

We denote the forward process corresponding to the m -th initial condition and solution by $\{x_n^m\}_{n=0}^T$, where $x_n^m := u^m(\mathbf{x}, t_n)$. We define the following datasets:

$$\begin{aligned} \mathbf{X} &= \{(x_0^m, t_n) \mid n = 1, \dots, T, \quad m = 1, \dots, M\} \\ \mathbf{Y} &= \{x_n^m \mid n = 1, \dots, T, \quad m = 1, \dots, M\} \end{aligned} \quad (12)$$

So, each solution of the PDE is transformed into T pairs of samples that correspond to the mapping described in (11).

3.3 DiTTO architecture

Using the formulation in Section 3.1, we present DiTTO: a diffusion-inspired temporal transformer operator, and describe its architecture. The network receives two main inputs: the initial condition $x_0 = u(\mathbf{x}, 0)$ and a time step $t = t_n$. Recall, that x_0 is a d -dimensional matrix, and t is a nonnegative scalar. The spatial and temporal inputs are treated differently throughout the forward pass of the network. For the temporal input t , we use an embedding mechanism based on the original Transformer positional encoding [17]:

$$\begin{aligned} PE_{(pos, 2i)} &= \sin\left(\frac{pos}{10000^{2i/d_{emb}}}\right), \\ PE_{(pos, 2i+1)} &= \cos\left(\frac{pos}{10000^{2i/d_{emb}}}\right), \end{aligned} \quad (13)$$

where d_{emb} is the desired embedding dimension. Each scalar t is mapped into a vector of size d_{emb} . Then this vector is passed through a simple feedforward neural network (FFN) with two linear layers and a GELU [34] activation function.

For the spatial input x_0 , we begin by concatenating it with the spatial grid on which it was discretized. The result is then passed through a U-Net [35]. We use a similar U-Net variant common in many diffusion models, such as DDPM [29]. It follows the backbone of PixelCNN++ [36], a U-Net based on a Wide ResNet [37, 38]. It comprises three downsampling convolutional blocks, one block in the latent space, and three upsampling blocks. During downsampling, we double the number of filters in each block, starting from 16, until we reach 128 filters in the latent space. When upsampling, we half the number of filters in each block until we get 16 again. Each block contains four convolutional layers with a filter size of 3. Each layer is followed by a group normalization [39] and a SiLU activation [34, 40]. Skip connections and attention [41, 17] layers are added after the second and fourth layers. For the attention layers, we use 4 attention heads of size 32.

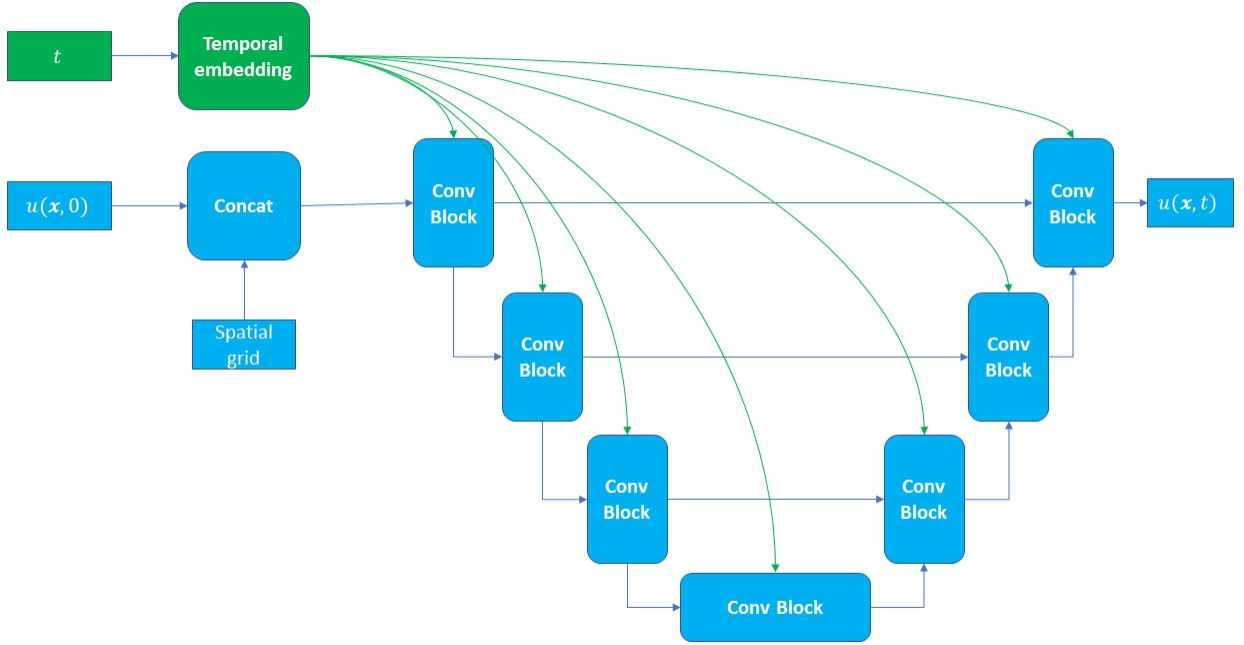


Figure 1: DiTTO architecture. The inputs are the discretized initial condition $u(\mathbf{x}, 0)$, its corresponding spatial grid, and the desired time $t \in \mathbb{R}^+$. The initial condition and the grid are concatenated and then inserted into a U-net with convolutional blocks. The time step t first passes through an embedding layer. Then, the resulting embedding is used to condition the network in each block.

The spatial and temporal inputs are connected in each block using a conditioning mechanism similar to Feature-wise Linear Modulation (FiLM) [42]. We begin by applying another FFN to the temporal embedding (13). The output of this FFN is two vectors, which we use to perform a scale and shift transformation. Specifically, the outputs of the first and third layers in each block are scaled by the first vector, and the second vector is then added to this result. This powerful conditioning mechanism enables the network to map the same initial condition into different values depending on the value of t . Moreover, it allows the network to receive continuous values for the temporal input t , making it entirely meshfree in time. The entire architecture is shown in Figure 1.

This architecture is not limited to a specific dimension. The same mechanism can be implemented for d -dimensional problems, where $d \in \{1, 2, 3\}$. The only major difference is the usage of d -dimensional convolutions for the relevant problem. The implementation relies on the following DDPM implementations: <https://github.com/lucidrains/denoising-diffusion-pytorch> and <https://github.com/lucidrains/video-diffusion-pytorch>. We refer to the original implementation for more details regarding the architecture.

3.4 Loss function

Let \mathcal{O}_θ be the neural network described in Section 3.3 with hyperparameters θ . The goal of \mathcal{O}_θ is to learn the mapping described in (11), using the dataset (12). We split this dataset into training, validation, and testing sets. We split them in a way that makes sure that no initial conditions from the validation and testing sets appear in the training set.

Difgetn models are often trained with a probabilistic loss function. However, since we learn a PDE operator, other loss functions commonly used for SciML applications are more fitting. Consequently, we train the network with a mean relative L^2 loss:

$$loss := \frac{1}{MT} \sum_{m=1}^M \sum_{n=1}^T \frac{\|\mathcal{O}_\theta(x_0^m, t_n) - x_n^m\|_2}{\varepsilon + \|x_n^m\|_2}, \quad (14)$$

where ε is a small number used to prevent a zero denominator and stabilize the loss. The inputs and outputs of the model are d -dimensional, so they are converted into a one-dimensional array by column stacking (flattening) inside the loss function when needed. We describe the loss for the entire dataset for simplicity, but in practice, we divide it into batches.

3.5 Faster sampling

Iterating over the entire dataset (12) can be time-consuming. For M_{train} initial conditions in the training set, we have $M_{train} \cdot T$ samples. So, the number of training steps scales linearly with T . This means the number of training samples is very large for fine temporal discretizations.

A similar problem occurs in generative diffusion models. The original DDPM [29] requires hundreds of forward passes to produce good results. Later works suggested ways to improve the performance aspect of DDPMs. For example, Song et al. [43] suggest using non-Markovian processes to improve the computational cost. Nichol et al. [33] present a way to significantly reduce the number of necessary steps by subsampling the original diffusion process. Both methods focus primarily on the inference speed. However, in the case of DiTTO, inference is immediate. In Section 3.1, we explained that we do not view x_0, x_1, \dots, x_T as an iterative process. Instead, we treat each sample individually, significantly increasing the inference speed compared to generative models such as DDPM. Hence, we focus on speeding up the training process.

We propose DiTTO-s, a faster variant of DiTTO that relies on a subsampling mechanism similar to [33]. Instead of iterating over the entire process, we iterate over a random subsequence. Recall that for the m -th initial condition in the training set, the full process is $\{x_n^m\}_{n=1}^T$. Instead, we take a set of random subsequences $S_m \subset \{0, 1, \dots, T\}$, such that $\sum_{m=1}^M |S_m| = \alpha MT$ for some $\alpha < 1$. For example, choosing $\alpha = 0.05$ means we only use 5% of the given samples in each epoch. The new DiTTO-s loss is given by:

$$loss_\alpha := \frac{1}{\alpha MT} \sum_{m=1}^M \sum_{n \in S_m} \frac{\|\mathcal{O}_\theta(x_0^m, t_n) - x_n^m\|_2}{\varepsilon + \|x_n^m\|_2}, \quad (15)$$

We note that after each epoch, we randomly sample S_m again using a uniform distribution. That way, given a sufficiently large number of epochs, we expect to cover a significant portion of samples in the dataset.

4 Results

We test the proposed DiTTO method on a wide variety of time-dependent PDEs in multiple dimensions. Specifically, we use the following PDEs: 1D Burgers' equation, 2D incompressible Navier-Stokes, 2D acoustic wave equation, and 3D acoustic wave equation. We compare the DiTTO method and its variant DiTTO-s in Section 3.5 to two other methods. First, we compare it to the popular FNO method [3]. We also conduct a comparison to a standard U-Net model with attention. We use the same U-Net architecture as in Section 3.3, except we remove all temporal conditioning. We compute the relative L^2 error for each method and compare it to the ground truth data.

We generate datasets containing solutions of the PDEs. We randomly sample 1,000 initial conditions and then use numerical solvers to find their corresponding solutions. Details regarding the data generation process and the solvers used for each problem are presented in the following sections. All models were trained on these datasets. In each case, the spatiotemporal resolution of the numerical solution is kept fixed. The spatial grid size, denoted by N_x, N_y , and N_z , is determined by the dimensionality of the problem. We use the same spatial grid for training and inference.

For the number of timesteps N_t (following standard PDE notation), we use different resolutions for training and inference to test the temporal interpolation and super-resolution capabilities of DiTTO. We train all models with $N_t^{train} = 50$ time steps, and test on $N_t^{test} \in \{10, 20, 50, 100, 200\}$. These choices of N_t^{test} allow us to examine the results in three different regimes. First, when $N_t^{test} = 50$, we test the model on the same temporal resolution it was trained on. We see how well the model handles coarser temporal grids for $N_t^{test} \in \{10, 20\}$. Finally, we consider a zero-shot super-resolution scenario in time for $N_t^{test} \in \{100, 200\}$, exploring the interpolation capabilities of the model on unseen temporal discretizations.

Note that DiTTO and DiTTO-s are entirely meshfree in time due to the time conditioning mechanism. Consequently, they do not require any temporal discretization. However, the ground-truth reference solutions for the above PDEs are generated using standard time-marching numerical solvers with fixed timestep sizes.

When training the FNOs, for comparison purposes, we encounter different behavior. In [3], Li et al. suggest two ways to add time dependency to FNOs. The first method takes a d -dimensional (in space) problem and uses a d -dimensional FNO in an auto-regressive manner to evolve the solution over time. This approach is not computationally viable due to the large number of timesteps required for training. The second approach transforms a d -dimensional problem in space to a $(d + 1)$ -dimensional spatiotemporal problem and uses a $(d + 1)$ -dimensional FNO to solve it. We use the latter approach due to computational and scalability aspects.

We train all models using the relative L^2 loss in Equation (14) for 500 epochs. We monitor the loss during training and save the models with the lowest validation loss. The optimizer we use is the Adam/AdamW optimizer [44, 45] with an initial learning rate 10^{-3} and weight decay 10^{-4} . The learning rate is updated throughout the training process using cosine annealing [46]. For DiTTO-s, we use a subsampling rate of $\alpha = 0.1$ as described in Section 3.5. For more details regarding the effect of α , we refer to Appendix A.3. In all examples, we provide a quantitative performance comparison using the relative L^2 error (shown in the tables) and a qualitative performance comparison for a randomly selected sample from the test set (shown in the figures).

4.1 1D Burgers' equation

The one-dimensional Burgers' equation for a viscous fluid is given by:

$$\begin{cases} \partial_t u(x, t) + \partial_x(u^2(x, t)/2) = \nu \partial_{xx} u(x, t), & x \in (0, 1), t \in (0, t_{final}] \\ u(x, 0) = u_0, & x \in (0, 1) \end{cases}, \quad (16)$$

where $\nu \in \mathbb{R}^+$ is the viscosity coefficient, and the PDE is subject to periodic boundary conditions. Note that this is a nonlinear equation that can develop shocks even for smooth initial conditions. The initial condition $u_0(x)$ is sampled from a Gaussian random field according to the following distribution: $\mathcal{N}(0, 625(-\Delta + 25I)^{-2})$, where \mathcal{N} is the normal distribution, and Δ, I are the Laplacian and identity operators, respectively.

We use the publicly available MATLAB [47] solver given in [3] to create three separate datasets with different parameters. The first dataset is created with $\nu = 0.01$, $t_{final} = 1$, and $N_x = 128$. This is a relatively simple scenario since these parameters produce smooth solutions without shocks. In the second dataset, we decrease the viscosity coefficient to $\nu = 0.001$, which increases the shock behavior of the Burgers' equation. For this reason, we also increase the spatial discretization to $N_x = 256$. Finally, the third dataset is the same as the second one, except we increase the final simulation time to $t_{final} = 2$, which causes the shocks to be more pronounced.

The results for the three scenarios are shown in Tables 1 to 3. DiTTO and DiTTO-s achieve the lowest errors for the three datasets. When $N_t^{test} = N_t^{train} = 50$, all methods have similar errors, with DiTTO and DiTTO-s having a slight advantage. However, when $N_t^{test} \neq N_t^{train}$, DiTTO and DiTTO-s significantly outperform the FNO and the U-Net. Moreover, we observe that the DiTTO and DiTTO-s results do not depend on the temporal discretization, as the errors stay roughly the same for all values of N_t^{test} . We also note that DiTTO-s has a slightly lower error than the full DiTTO. This demonstrates that the subsampling mechanism does not only require fewer training steps but also improves the model. The reason for this is that the subsampling mechanism acts as a form of regularization that helps decrease the error. In Figure 2, we present a visual comparison of the various methods for the third dataset. We refer to Appendix A.1 for similar figures regarding the other cases.

	$N_t^{test} = 10$	$N_t^{test} = 20$	$N_t^{test} = 50$	$N_t^{test} = 100$	$N_t^{test} = 200$
DiTTO	0.0060	0.0059	0.0058	0.0065	0.0070
DiTTO-s	0.0057	0.0056	0.0055	0.0061	0.0066
FNO	0.1672	0.0217	0.0059	0.0100	0.0124
U-Net	0.4096	0.1668	0.0094	0.1017	0.1782

Table 1: Relative L^2 test set errors for the Burgers' scenario in Section 4.1 with $t_{final} = 1$, $\nu = 0.01$, $N_x = 128$, $N_t^{train} = 50$.

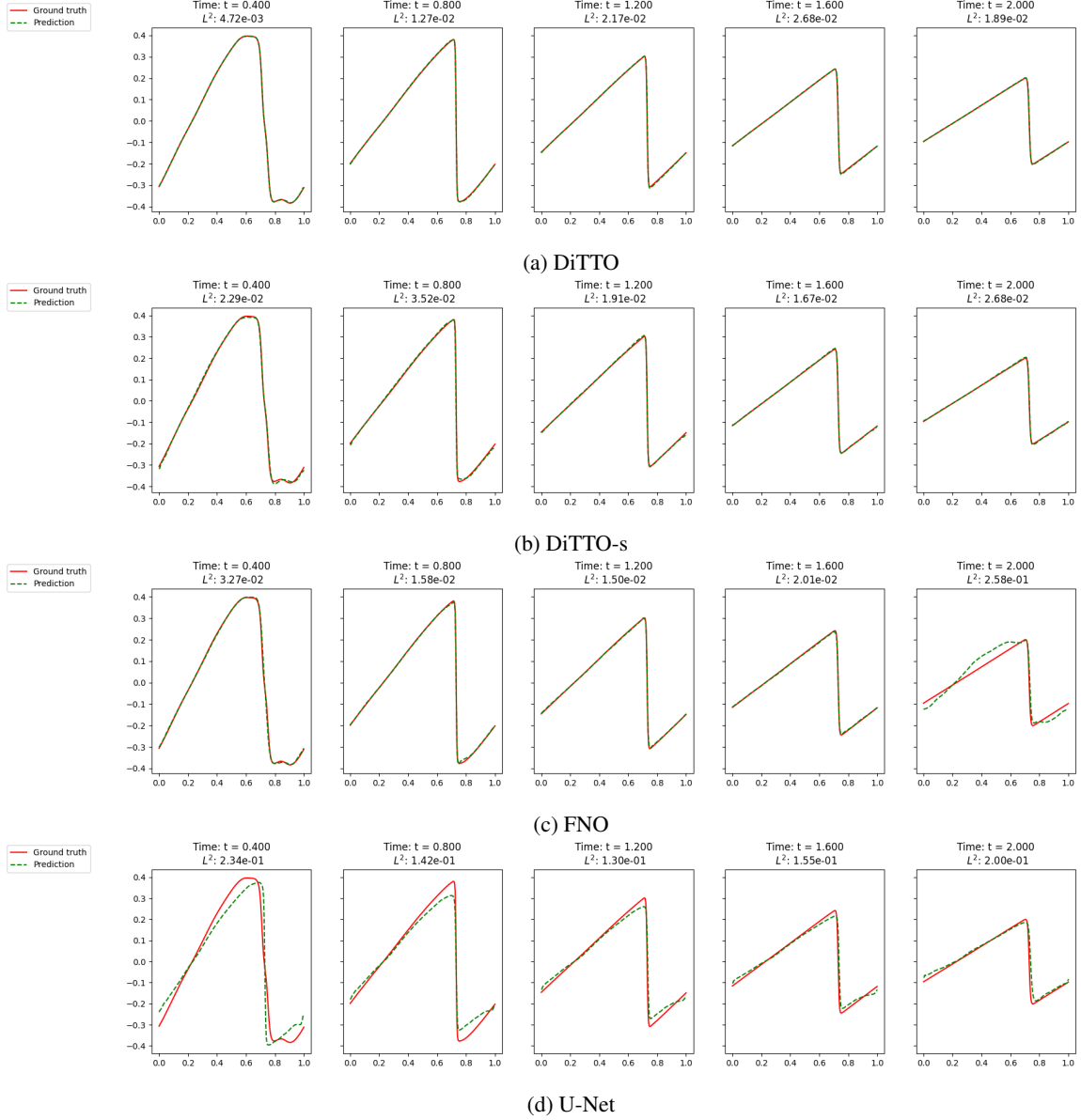


Figure 2: Results for the Burgers' problem described in Section 4.1 with $\nu = 0.001$, $t_{final} = 2$, $N_x = 256$, $N_t^{train} = 50$, and $N_t^{test} = 200$, for a random initial condition from the test set. In Figures 2a to 2d, we see a comparison between the models at different times. We plot the predictions of the models alongside the reference solution (ground truth).

	$N_t^{test} = 10$	$N_t^{test} = 20$	$N_t^{test} = 50$	$N_t^{test} = 100$	$N_t^{test} = 200$
DiTTO	0.0164	0.0157	0.0154	0.0153	0.0152
DiTTO-s	0.0124	0.0119	0.0116	0.0116	0.0116
FNO	0.2899	0.0461	0.0222	0.0265	0.0299
U-Net	0.4789	0.2807	0.0298	0.2042	0.3188

Table 2: Relative L^2 test set errors for the Burgers’ scenario in Section 4.1 with $t_{final} = 1$, $\nu = 0.001$, $N_x = 256$, $N_t^{train} = 50$.

	$N_t^{test} = 10$	$N_t^{test} = 20$	$N_t^{test} = 50$	$N_t^{test} = 100$	$N_t^{test} = 200$
DiTTO	0.0208	0.0199	0.0195	0.0195	0.0196
DiTTO-s	0.0172	0.0164	0.0160	0.0160	0.0161
FNO	0.3501	0.0582	0.0248	0.0315	0.0367
U-Net	0.6655	0.3795	0.0382	0.2426	0.3167

Table 3: Relative L^2 test set errors for the Burgers’ scenario in Section 4.1 with $t_{final} = 2$, $\nu = 0.001$, $N_x = 256$, $N_t^{train} = 50$.

4.2 2D Navier-Stokes equation

The time-dependent two-dimensional Navier-Stokes equation for the viscous, incompressible fluid in vorticity form is given by:

$$\begin{cases} \partial_t \omega(x, y, t) + u(x, y, t) \cdot \nabla \omega(x, y, t) = \nu \Delta \omega(x, y, t) + f(x, y), & x, y \in (0, 1)^2, t \in (0, t_{final}] \\ \nabla \cdot u(x, y, t) = 0, & (x, y) \in (0, 1)^2, t \in (0, t_{final}] \\ \omega(x, y, 0) = \omega_0, & (x, y) \in (0, 1)^2 \end{cases} \quad (17)$$

where ω is the vorticity, u is the velocity field, ν is the viscosity, and Δ is the two-dimensional Laplacian operator. We consider periodic boundary conditions here as well. The source term f is chosen as $f(x, y) = 0.1(\sin(2\pi(x + y)) + \cos(2\pi(x + y)))$, and the initial condition $\omega_0(x)$ is sampled from a Gaussian random field according to the distribution $\mathcal{N}(0, 7^{3/2}(-\Delta + 49I)^{-5/2})$.

We use the publicly available Python solver given in [3] to generate two datasets with a spatial resolution of $N_x = N_y = 64$. The first dataset is created with $\nu = 10^{-3}$ and $t_{final} = 50$, resulting in a Reynolds number $Re \approx 20$. For the second dataset we use $\nu = 10^{-5}$ and $t_{final} = 20$, resulting in a Reynolds number $Re \approx 2,000$.

The error comparison for the two datasets is shown in Table 4 and Table 5, respectively. In Table 4, we see that for $Re \approx 20$, both DiTTO and DiTTO-s outperform the other models across all temporal discretizations while keeping similar error values. In Table 5, we see the results for $Re \approx 2,000$. It is clear that increasing the Reynolds number also increases the difficulty of the problem, as evidenced by the noticeably higher errors for all models. We also see that the FNO errors are closer to DiTTO-s compared to other cases, even having a slight advantage when $N_t^{test} \in \{50, 100\}$. In Figures 3 and 4, we present a visual comparison of the various methods for both of the Navier-Stokes scenarios using one of the initial conditions from the test set. In both figures we see that the standard U-Net cannot interpolate in time, unlike the other methods.

	$N_t^{test} = 10$	$N_t^{test} = 20$	$N_t^{test} = 50$	$N_t^{test} = 100$	$N_t^{test} = 200$
DiTTO	0.0344	0.0334	0.0328	0.0327	0.0328
DiTTO-s	0.0334	0.0323	0.0318	0.0316	0.0316
FNO	0.3731	0.1430	0.0511	0.0646	0.0788
U-Net	0.6289	0.7379	0.0595	0.6416	0.5884

Table 4: Relative L^2 test set errors for the Navier-Stokes scenario in Section 4.2 with $\nu = 10^{-3}$, $t_{final} = 50$, $Re \approx 20$, $N_x = N_y = 64$.

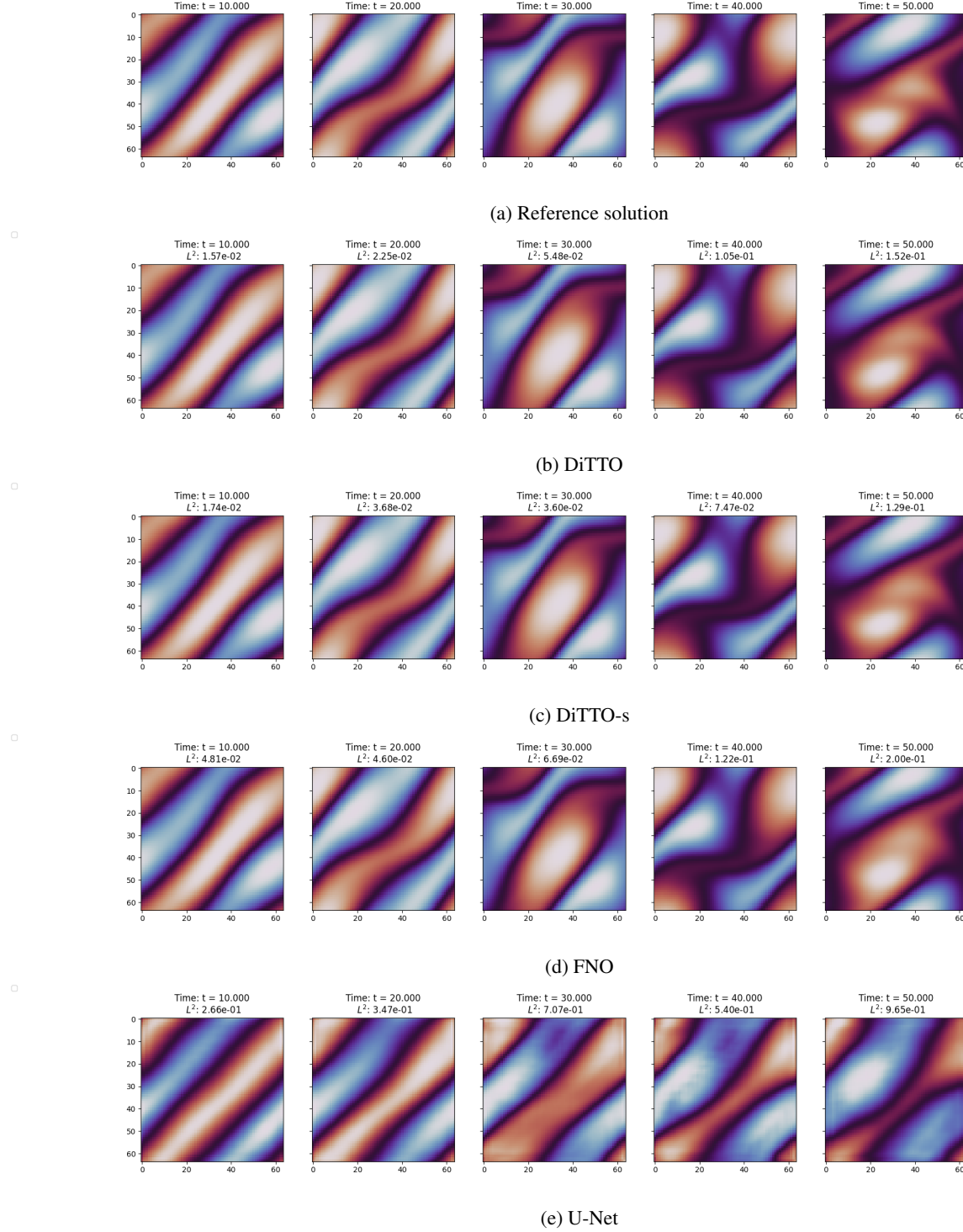


Figure 3: Results for the Navier-Stokes scenario described in Section 4.2 with $\nu = 10^{-3}$, $t_{final} = 50$, and $Re \approx 20$. The results are evaluated at different times for a random initial condition. In Figure 3a, we see the reference solution obtained via a numerical solver. In Figures 3b to 3e, we see the predictions of the models and their errors for the case $N_t^{train} = 50$ and $N_t^{test} = 200$.

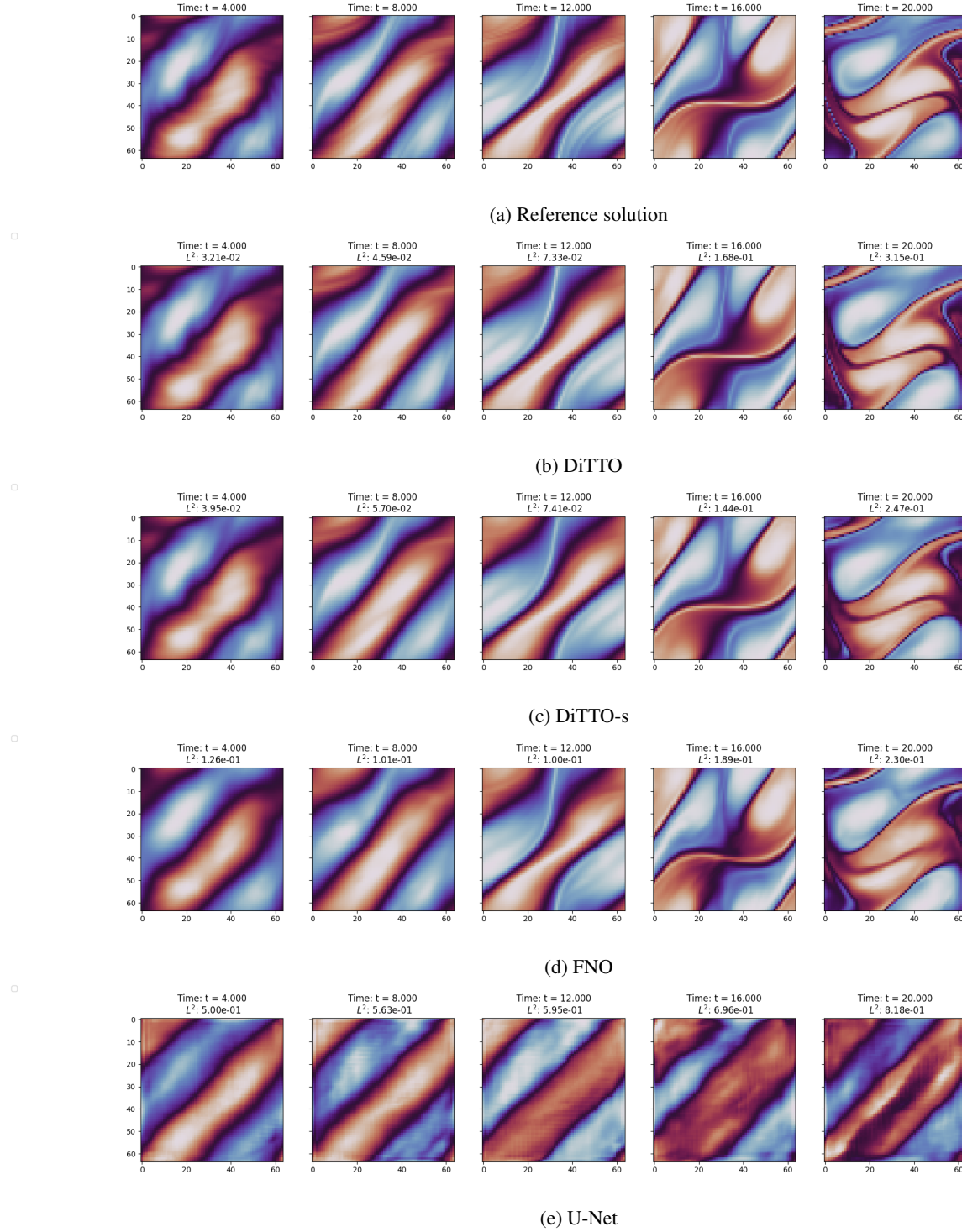


Figure 4: Results for the Navier-Stokes scenario described in Section 4.2 with $\nu = 10^{-5}$, $t_{final} = 20$, and $Re \approx 2,000$. The results are evaluated at different times for a random initial condition. In Figure 4a, we see the reference solution obtained via a numerical solver. In Figures 4b to 4e, we see the predictions of the models and their errors for the case $N_t^{train} = 50$ and $N_t^{test} = 200$.

	$N_t^{test} = 10$	$N_t^{test} = 20$	$N_t^{test} = 50$	$N_t^{test} = 100$	$N_t^{test} = 200$
DiTTO	0.2030	0.1887	0.1800	0.1770	0.1755
DiTTO-s	0.1874	0.1749	0.1668	0.1641	0.1628
FNO	0.3200	0.2034	0.1582	0.1635	0.1700
U-Net	0.7287	0.7184	0.2028	0.7046	0.6802

Table 5: Relative L^2 test set errors for the Navier-Stokes scenario in Section 4.2 with $\nu = 10^{-5}$, $t_{final} = 20$, $Re \approx 2,000$, $N_x = N_y = 64$.

4.3 2D Wave equation

We consider the following formulation of the acoustic wave equation in two dimensions [48, 49]:

$$\begin{cases} u_{tt}(x, y, t) = c^2(x, y)(u_{xx}(x, y, t) + u_{yy}(x, y, t)) & (x, y) \in (0, L)^2; 0 \leq t \leq t_{final}, \\ u(x, y, 0) = u_0(x, y) & (x, y) \in (0, L)^2, \\ u_t(x, y, 0) = 0 & (x, y) \in (0, L)^2, \\ u(0, y, t) = u(L, y, t) = 0 & y \in (0, L), 0 \leq t \leq t_{final}, \\ u(x, 0, t) = u(x, L, t) = 0 & x \in (0, L), 0 \leq t \leq t_{final}. \end{cases} \quad (18)$$

where $u(x, y, t)$ is the wave amplitude or acoustic pressure, $c(x, y) = (1 + \sin(x) \sin(y))$ is the wave propagation speed, $t_{final} = 2$ is the final propagation time, and $L = \pi$ is the size of the physical domain. The initial condition u_0 is chosen to be a Gaussian source of the form:

$$u(x, y, 0) = e^{-\left(\frac{(x-x_c)^2 + (y-y_c)^2}{10}\right)}. \quad (19)$$

To create the dataset, we generate several initial conditions of the same type, randomly varying the spatial location (x_c, y_c) of the center of the source. The locations are sampled using a discrete random uniform distribution on the indices of the grid. We generate the numerical solutions using a finite-difference numerical scheme with a grid of $N_x = N_y = 64$ spatial nodes.

The results are shown in Table 6. DiTTO and DiTTO-s both achieve the lowest errors. We note that the FNO and the U-Net fare much worse compared to the other PDEs when changing discretization. Specifically, the errors of DiTTO and DiTTO-s are an order of magnitude lower the FNO. We hypothesize that this might be related to the use of Dirichlet boundary conditions instead of periodic ones. Another reason might be the sparsity of the data in this case, which causes the solution to change rapidly over time and have sharp features (see Figure 5).

	$N_t^{test} = 10$	$N_t^{test} = 20$	$N_t^{test} = 50$	$N_t^{test} = 100$	$N_t^{test} = 200$
DiTTO	0.0159	0.0150	0.0137	0.0392	0.0460
DiTTO-s	0.0239	0.0250	0.0204	0.0396	0.0407
FNO	1.2238	0.4186	0.0818	0.1728	0.2348
U-Net	1.6576	1.3890	0.0702	1.2300	1.2896

Table 6: Relative L^2 test set errors for the 2D wave equation described in Section 4.3.

4.4 3D Wave equation

Similarly to (18), the formulation of the acoustic wave equation in three dimensions is given by:

$$\begin{cases} u_{tt}(x, y, z, t) = c^2(x, y, z)(u_{xx}(x, y, z, t) + u_{yy}(x, y, z, t) + u_{zz}(x, y, z, t)) & (x, y, z) \in (0, L)^3; 0 \leq t \leq t_{final}, \\ u(x, y, z, 0) = u_0(x, y, z) & (x, y, z) \in (0, L)^3, \\ u_t(x, y, z, 0) = 0 & (x, y, z) \in (0, L)^3, \\ u(0, y, z, t) = u(L, y, z, t) = 0 & (y, z) \in (0, L)^2, 0 \leq t \leq t_{final}, \\ u(x, 0, z, t) = u(x, L, z, t) = 0 & (x, z) \in (0, L)^2, 0 \leq t \leq t_{final}, \\ u(x, y, 0, t) = u(x, y, L, t) = 0 & (x, y) \in (0, L)^2, 0 \leq t \leq t_{final}. \end{cases} \quad (20)$$

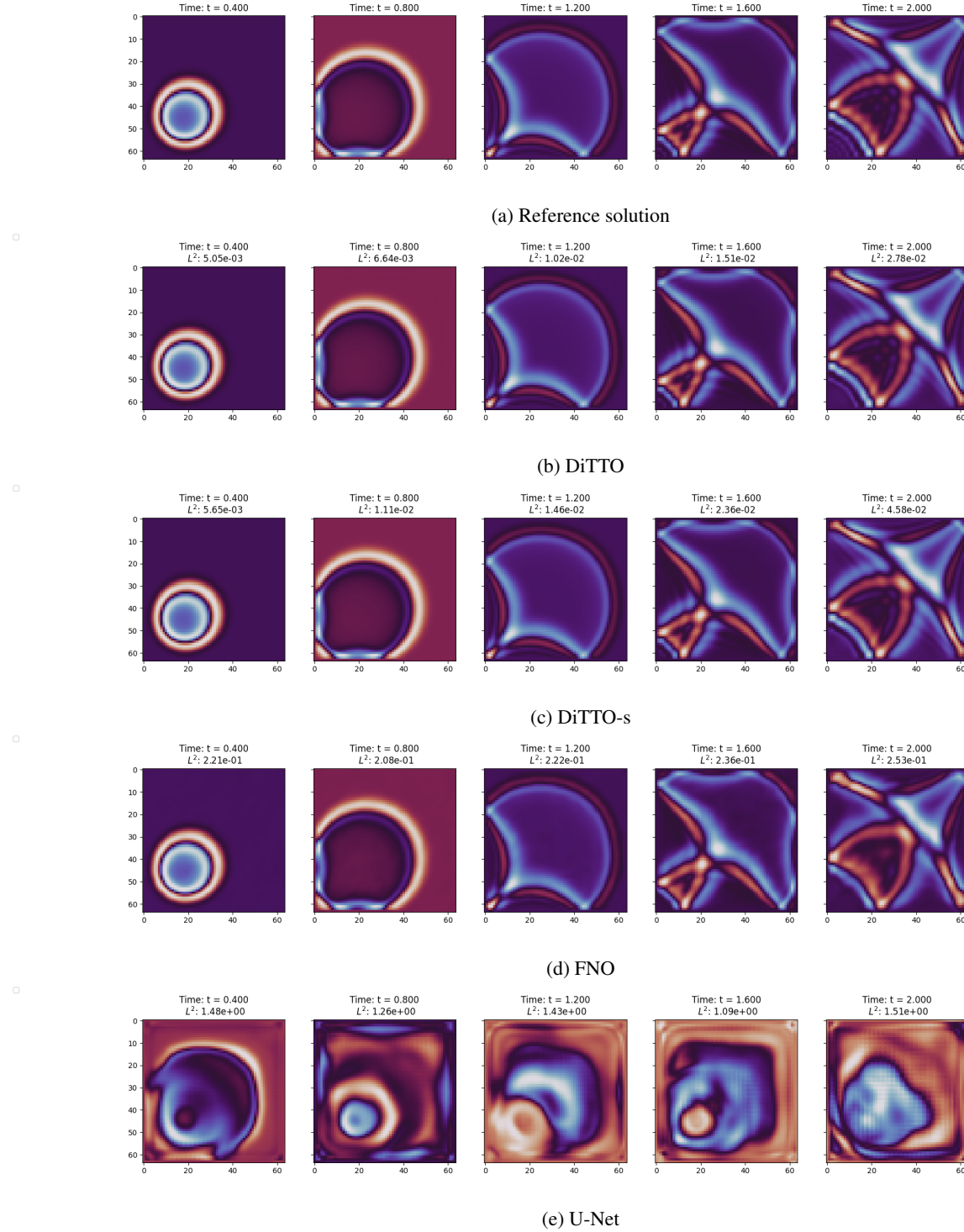


Figure 5: Results for the 2D wave equation described in Section 4.3 at different times for a random initial condition from the test set. In Figure 5a, we see the reference solution obtained via a numerical solver. In Figures 5b to 5e, we see the predictions of the models and their errors for the case $N_t^{train} = 50$ and $N_t^{test} = 200$.

We generate the initial conditions u_0 in the same way as the two-dimensional case in Equation (19), except we now define them on a three-dimensional grid:

$$u(x, y, z, 0) = e^{-\left(\frac{(x-x_c)^2 + (y-y_c)^2 + (z-z_c)^2}{10}\right)}. \quad (21)$$

We keep $t_{final} = 2$, $L = \pi$, and choose $c(x, y, z) = (1 + \sin(2x) \sin(y) \sin(z))$ to be the velocity. We generate the corresponding numerical solutions using a finite-difference numerical scheme with a grid of $N_x = N_y = N_z = 32$ spatial nodes.

Note that for the three-dimensional case, we only use DiTTO and DiTTO-s. Since this is a time-dependent problem, we need a four-dimensional U-Net and a four-dimensional FNO, which are prohibitively expensive and not easily implemented. The results are shown in Table 7. Similarly to the other experiments, DiTTO and DiTTO-s maintain similar error values over the different temporal discretizations. A visual example using a random initial condition is shown in Figure 6. We note that the computational grid in this scenario is significantly larger. It has 32,768 nodes in space, with a maximum $N_t^{test} = 200$, effectively increasing the number of spatio-temporal nodes to approximately 6.5 million. We observe the low error values of the DiTTO models, showing excellent performance even for a large-scale three-dimensional problem, as seen in Figure 6.

	$N_t^{test} = 10$	$N_t^{test} = 20$	$N_t^{test} = 50$	$N_t^{test} = 100$	$N_t^{test} = 200$
DiTTO	0.1850	0.1885	0.1801	0.1828	0.1821
DiTTO-s	0.1829	0.1830	0.1816	0.1819	0.1818

Table 7: Relative L^2 test set errors for the 3D wave equation described in Section 4.4.

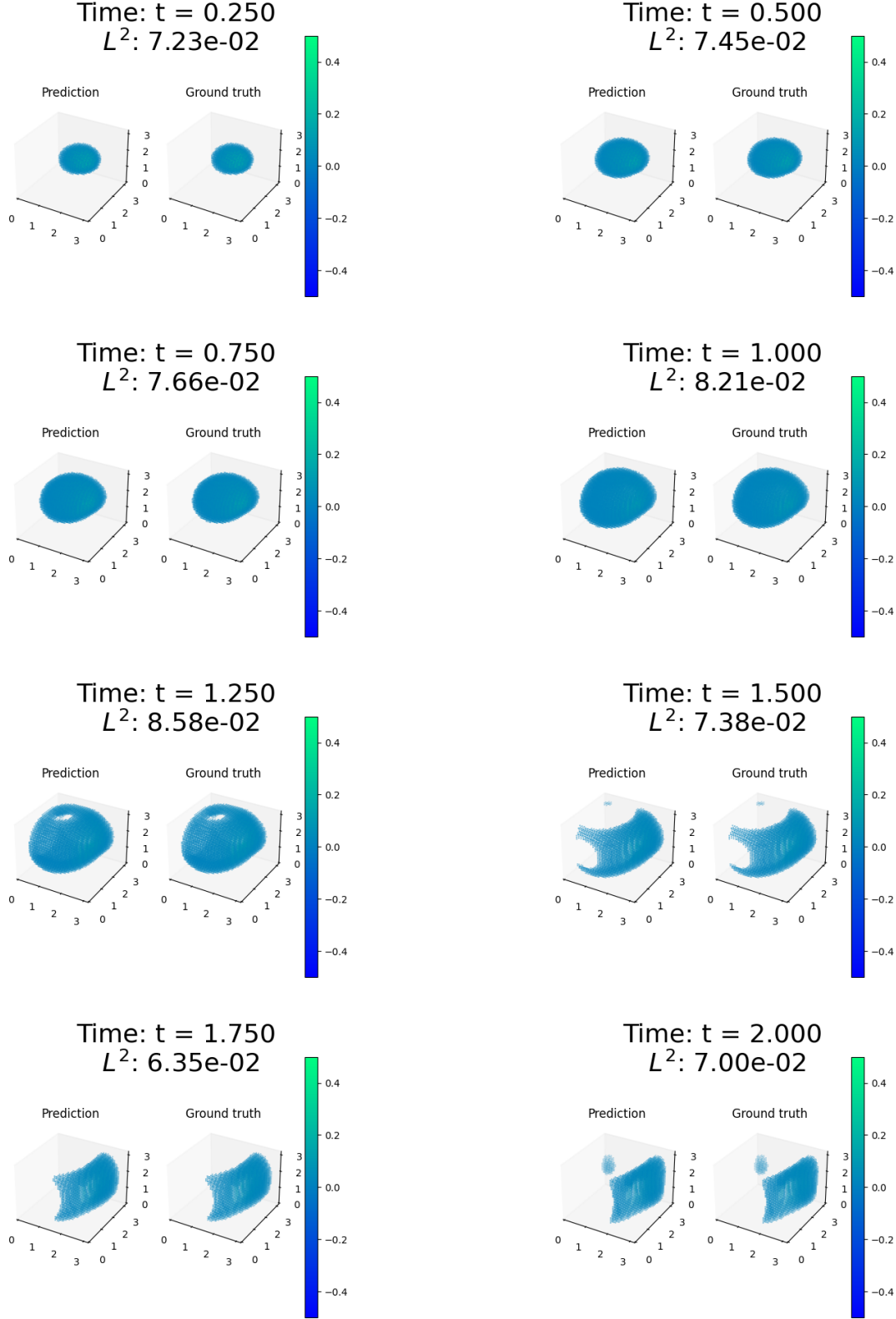


Figure 6: DiTTO results for the 3D wave equation described in Section 4.4 at different times for a random initial condition from the test set. In each figure, the predicted and reference solutions (ground-truth) are shown side-by-side, along with the relative error between them for the case $N_t^{train} = 50$ and $N_t^{test} = 200$.

5 Discussion and future work

We have presented a novel approach to solving PDEs in a data-driven way. This method, named DiTTO, combines elements from diffusion models and the Transformer architecture. We have shown that DiTTO achieves state-of-the-art results for a wide variety of PDEs in multiple dimensions. Moreover, the proposed method was shown to have strong grid independence in the time domain. Consequently, DiTTO can make accurate predictions at arbitrary timesteps without retraining.

We believe that the capabilities of DiTTO can be further expanded upon. Since this approach has shown excellent time interpolation capabilities, extending it to extrapolation problems is a natural course of action. Furthermore, adding physics-informed elements to the method could further enhance its potential. Finally, utilizing theoretical results from the fields of diffusion models and conditioning in deep learning could help us provide a theoretical background for DiTTO.

References

- [1] M. Raissi, P. Perdikaris, and G.E. Karniadakis. Physics-informed neural networks: A deep learning framework for solving forward and inverse problems involving nonlinear partial differential equations. *Journal of Computational Physics*, 378:686–707, 2019.
- [2] Lu Lu, Pengzhan Jin, Guofei Pang, Zhongqiang Zhang, and George Em Karniadakis. Learning nonlinear operators via deepnet based on the universal approximation theorem of operators. *Nature machine intelligence*, 3(3):218–229, 2021.
- [3] Zongyi Li, Nikola Kovachki, Kamyar Azizzadenesheli, Burigede Liu, Kaushik Bhattacharya, Andrew Stuart, and Anima Anandkumar. Fourier neural operator for parametric partial differential equations. *arXiv preprint arXiv:2010.08895*, 2020.
- [4] Zichao Long, Yiping Lu, Xianzhong Ma, and Bin Dong. Pde-net: Learning pdes from data. In *International conference on machine learning*, pages 3208–3216. PMLR, 2018.
- [5] Hao Xu, Haibin Chang, and Dongxiao Zhang. Dl-pde: Deep-learning based data-driven discovery of partial differential equations from discrete and noisy data. *arXiv preprint arXiv:1908.04463*, 2019.
- [6] Tribikram Kundu. Acoustic source localization. *Ultrasonics*, 54(1):25–38, 2014.
- [7] Oded Ovadia, Adar Kahana, Eli Turkel, and Shai Dekel. Beyond the courant-friedrichs-lewy condition: Numerical methods for the wave problem using deep learning. *Journal of Computational Physics*, 442:110493, 2021.
- [8] Shengze Cai, Zhiping Mao, Zhicheng Wang, Minglang Yin, and George Em Karniadakis. Physics-informed neural networks (pinns) for fluid mechanics: A review. *Acta Mechanica Sinica*, 37(12):1727–1738, 2021.
- [9] Enrui Zhang, Adar Kahana, Eli Turkel, Rishikesh Ranade, Jay Pathak, and George Em Karniadakis. A hybrid iterative numerical transferable solver (hints) for pdes based on deep operator network and relaxation methods. *arXiv preprint arXiv:2208.13273*, 2022.
- [10] Anthony T Patera. A spectral element method for fluid dynamics: laminar flow in a channel expansion. *Journal of Computational Physics*, 54(3):468–488, 1984.
- [11] John Kim, Parviz Moin, and Robert Moser. Turbulence statistics in fully developed channel flow at low Reynolds number. *Journal of Fluid Mechanics*, 177:133–166, 1987.
- [12] Reinoud Sleeman and Torild Van Eck. Robust automatic p-phase picking: an on-line implementation in the analysis of broadband seismogram recordings. *Physics of the earth and planetary interiors*, 113(1-4):265–275, 1999.
- [13] Oded Ovadia, Adar Kahana, Panos Stinis, Eli Turkel, and George Em Karniadakis. Vito: Vision transformer-operator. *arXiv preprint arXiv:2303.08891*, 2023.
- [14] Jacques Hadamard. Sur les problèmes aux dérivées partielles et leur signification physique. *Princeton university bulletin*, pages 49–52, 1902.
- [15] Nikola B. Kovachki, Zongyi Li, Burigede Liu, Kamyar Azizzadenesheli, Kaushik Bhattacharya, Andrew M. Stuart, and Anima Anandkumar. Neural operator: Learning maps between function spaces. *CoRR*, abs/2108.08481, 2021.
- [16] Lu Lu, Xuhui Meng, Shengze Cai, Zhiping Mao, Somdatta Goswami, Zhongqiang Zhang, and George Em Karniadakis. A comprehensive and fair comparison of two neural operators (with practical extensions) based on fair data. *Computer Methods in Applied Mechanics and Engineering*, 393:114778, 2022.

- [17] Ashish Vaswani, Noam Shazeer, Niki Parmar, Jakob Uszkoreit, Llion Jones, Aidan N Gomez, Łukasz Kaiser, and Illia Polosukhin. Attention is all you need. *Advances in neural information processing systems*, 30, 2017.
- [18] Qingsong Wen, Tian Zhou, Chaoli Zhang, Weiqi Chen, Ziqing Ma, Junchi Yan, and Liang Sun. Transformers in time series: A survey. *arXiv preprint arXiv:2202.07125*, 2022.
- [19] Kai Han, Yunhe Wang, Hanting Chen, Xinghao Chen, Jianyuan Guo, Zhenhua Liu, Yehui Tang, An Xiao, Chunjing Xu, Yixing Xu, et al. A survey on vision transformer. *IEEE transactions on pattern analysis and machine intelligence*, 45(1):87–110, 2022.
- [20] Alexey Dosovitskiy, Lucas Beyer, Alexander Kolesnikov, Dirk Weissenborn, Xiaohua Zhai, Thomas Unterthiner, Mostafa Dehghani, Matthias Minderer, Georg Heigold, Sylvain Gelly, et al. An image is worth 16x16 words: Transformers for image recognition at scale. *arXiv preprint arXiv:2010.11929*, 2020.
- [21] Zijie Li, Kazem Meidani, and Amir Barati Farimani. Transformer for partial differential equations’ operator learning. *arXiv preprint arXiv:2205.13671*, 2022.
- [22] Xinliang Liu, Bo Xu, and Lei Zhang. Ht-net: Hierarchical transformer based operator learning model for multiscale pdes. *arXiv preprint arXiv:2210.10890*, 2022.
- [23] Zhongkai Hao, Chengyang Ying, Zhengyi Wang, Hang Su, Yinpeng Dong, Songming Liu, Ze Cheng, Jun Zhu, and Jian Song. Gnot: A general neural operator transformer for operator learning. *arXiv preprint arXiv:2302.14376*, 2023.
- [24] Zhongkai Hao, Zhengyi Wang, Hang Su, Chengyang Ying, Yinpeng Dong, Songming Liu, Ze Cheng, Jian Song, and Jun Zhu. Gnot: A general neural operator transformer for operator learning. In *International Conference on Machine Learning*, pages 12556–12569. PMLR, 2023.
- [25] Shuhao Cao. Choose a transformer: Fourier or galerkin. *Advances in neural information processing systems*, 34:24924–24940, 2021.
- [26] Ruchi Guo, Shuhao Cao, and Long Chen. Transformer meets boundary value inverse problems. *arXiv preprint arXiv:2209.14977*, 2022.
- [27] Varun Kumar, Leonard Gleyzer, Adar Kahana, Khemraj Shukla, and George Em Karniadakis. Crunchgpt: A chatgpt assisted framework for scientific machine learning. *arXiv preprint arXiv:2306.15551*, 2023.
- [28] Jascha Sohl-Dickstein, Eric Weiss, Niru Maheswaranathan, and Surya Ganguli. Deep unsupervised learning using nonequilibrium thermodynamics. In *International Conference on Machine Learning*, pages 2256–2265. PMLR, 2015.
- [29] Jonathan Ho, Ajay Jain, and Pieter Abbeel. Denoising diffusion probabilistic models. *Advances in Neural Information Processing Systems*, 33:6840–6851, 2020.
- [30] Ting Wang, Petr Plechac, and Jaroslaw Knap. Generative diffusion learning for parametric partial differential equations. *arXiv preprint arXiv:2305.14703*, 2023.
- [31] Dule Shu, Zijie Li, and Amir Barati Farimani. A physics-informed diffusion model for high-fidelity flow field reconstruction. *Journal of Computational Physics*, 478:111972, 2023.
- [32] Yue Liu, Zhengwei Yang, Zhenyao Yu, Zitu Liu, Dahui Liu, Hailong Lin, Mingqing Li, Shuchang Ma, Maxim Avdeev, and Siqi Shi. Generative artificial intelligence and its applications in materials science: Current situation and future perspectives. *Journal of Materiomics*, 2023.
- [33] Alexander Quinn Nichol and Prafulla Dhariwal. Improved denoising diffusion probabilistic models. In *International Conference on Machine Learning*, pages 8162–8171. PMLR, 2021.
- [34] Dan Hendrycks and Kevin Gimpel. Gaussian error linear units (gelus). *arXiv preprint arXiv:1606.08415*, 2016.
- [35] Olaf Ronneberger, Philipp Fischer, and Thomas Brox. U-net: Convolutional networks for biomedical image segmentation. In *Medical Image Computing and Computer-Assisted Intervention–MICCAI 2015: 18th International Conference, Munich, Germany, October 5-9, 2015, Proceedings, Part III* 18, pages 234–241. Springer, 2015.
- [36] Tim Salimans, Andrej Karpathy, Xi Chen, and Diederik P Kingma. Pixelcnn++: Improving the pixelcnn with discretized logistic mixture likelihood and other modifications. *arXiv preprint arXiv:1701.05517*, 2017.
- [37] Sergey Zagoruyko and Nikos Komodakis. Wide residual networks. *arXiv preprint arXiv:1605.07146*, 2016.
- [38] Kaiming He, Xiangyu Zhang, Shaoqing Ren, and Jian Sun. Deep residual learning for image recognition. In *Proceedings of the IEEE conference on computer vision and pattern recognition*, pages 770–778, 2016.
- [39] Yuxin Wu and Kaiming He. Group normalization. In *Proceedings of the European conference on computer vision (ECCV)*, pages 3–19, 2018.

- [40] Stefan Elfwing, Eiji Uchibe, and Kenji Doya. Sigmoid-weighted linear units for neural network function approximation in reinforcement learning. *Neural networks*, 107:3–11, 2018.
- [41] Tri Dao, Daniel Y. Fu, Stefano Ermon, Atri Rudra, and Christopher Ré. FlashAttention: Fast and memory-efficient exact attention with IO-awareness. In *Advances in Neural Information Processing Systems*, 2022.
- [42] Ethan Perez, Florian Strub, Harm De Vries, Vincent Dumoulin, and Aaron Courville. Film: Visual reasoning with a general conditioning layer. In *Proceedings of the AAAI conference on artificial intelligence*, volume 32, 2018.
- [43] Jiaming Song, Chenlin Meng, and Stefano Ermon. Denoising diffusion implicit models. *arXiv preprint arXiv:2010.02502*, 2020.
- [44] Diederik P Kingma and Jimmy Ba. Adam: A method for stochastic optimization. *arXiv preprint arXiv:1412.6980*, 2014.
- [45] Ilya Loshchilov and Frank Hutter. Decoupled weight decay regularization. *arXiv preprint arXiv:1711.05101*, 2017.
- [46] Ilya Loshchilov and Frank Hutter. Sgdr: Stochastic gradient descent with warm restarts. *arXiv preprint arXiv:1608.03983*, 2016.
- [47] The MathWorks Inc. Matlab version: 9.13.0 (r2022b), 2022.
- [48] Lawrence C Evans. *Partial differential equations*, volume 19. American Mathematical Society, 2022.
- [49] Jürgen Jost. *Partial differential equations*, volume 214. Springer Science & Business Media, 2012.

A Appendix

A.1 Full Burgers' equation results

In Section 4.1, we presented figures for the most difficult Burgers' case with $\nu = 0.001$, $t_{final} = 2$, and $N_x = 256$. Here we add figures for the two other cases: $\nu = 0.01$, $t_{final} = 1$, $N_x = 128$, and $\nu = 0.001$, $t_{final} = 2$, $N_x = 256$. Both cases involve zero-shot super-resolution in time with $N_t^{train} = 50$ and $N_t^{test} = 200$.

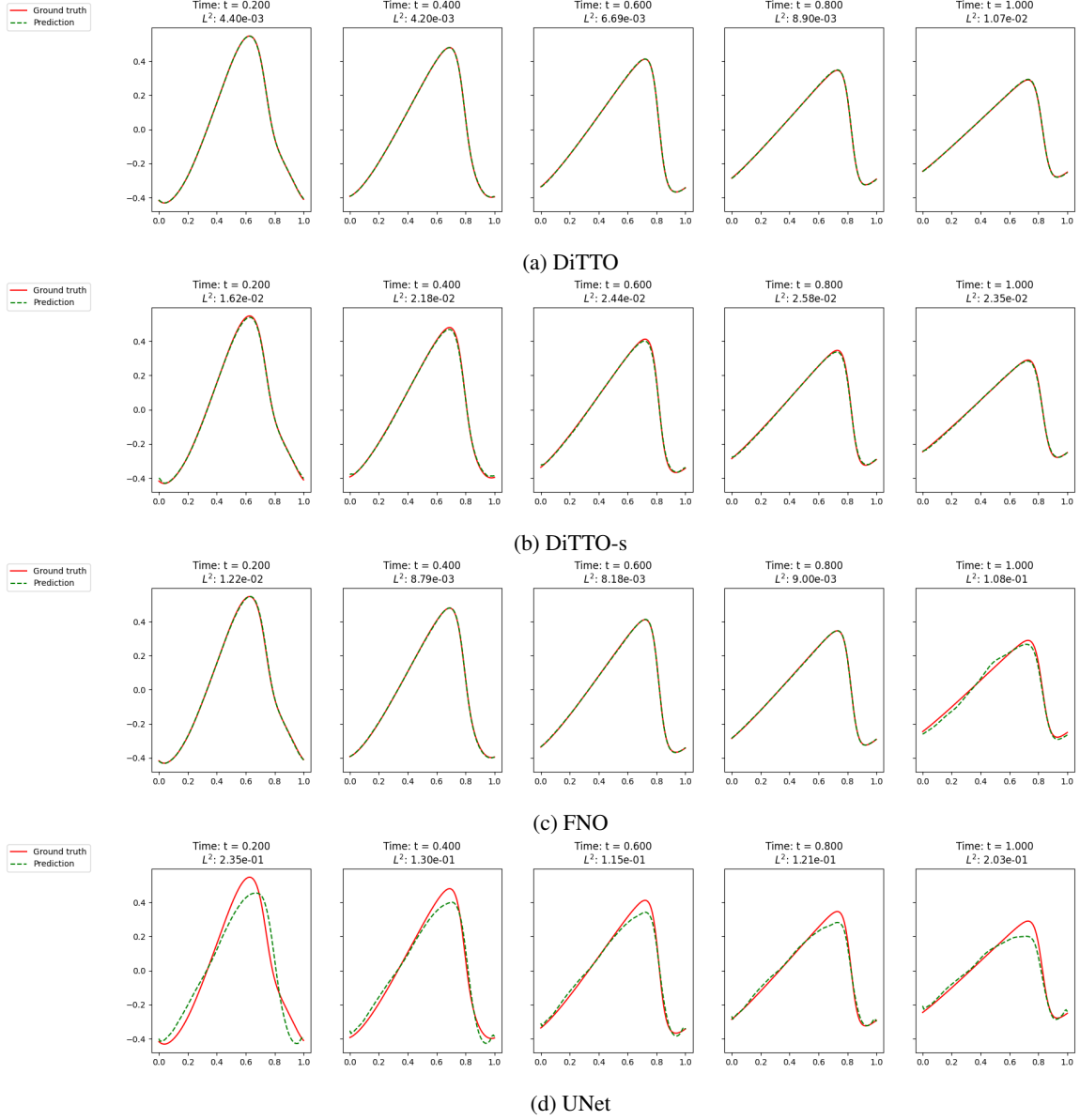


Figure 7: Burgers' scenario as described in Section 4.1 with $t_{final} = 1$, $\nu = 0.01$, $N_x = 128$, $N_t^{train} = 50$, and $N_t^{test} = 200$.

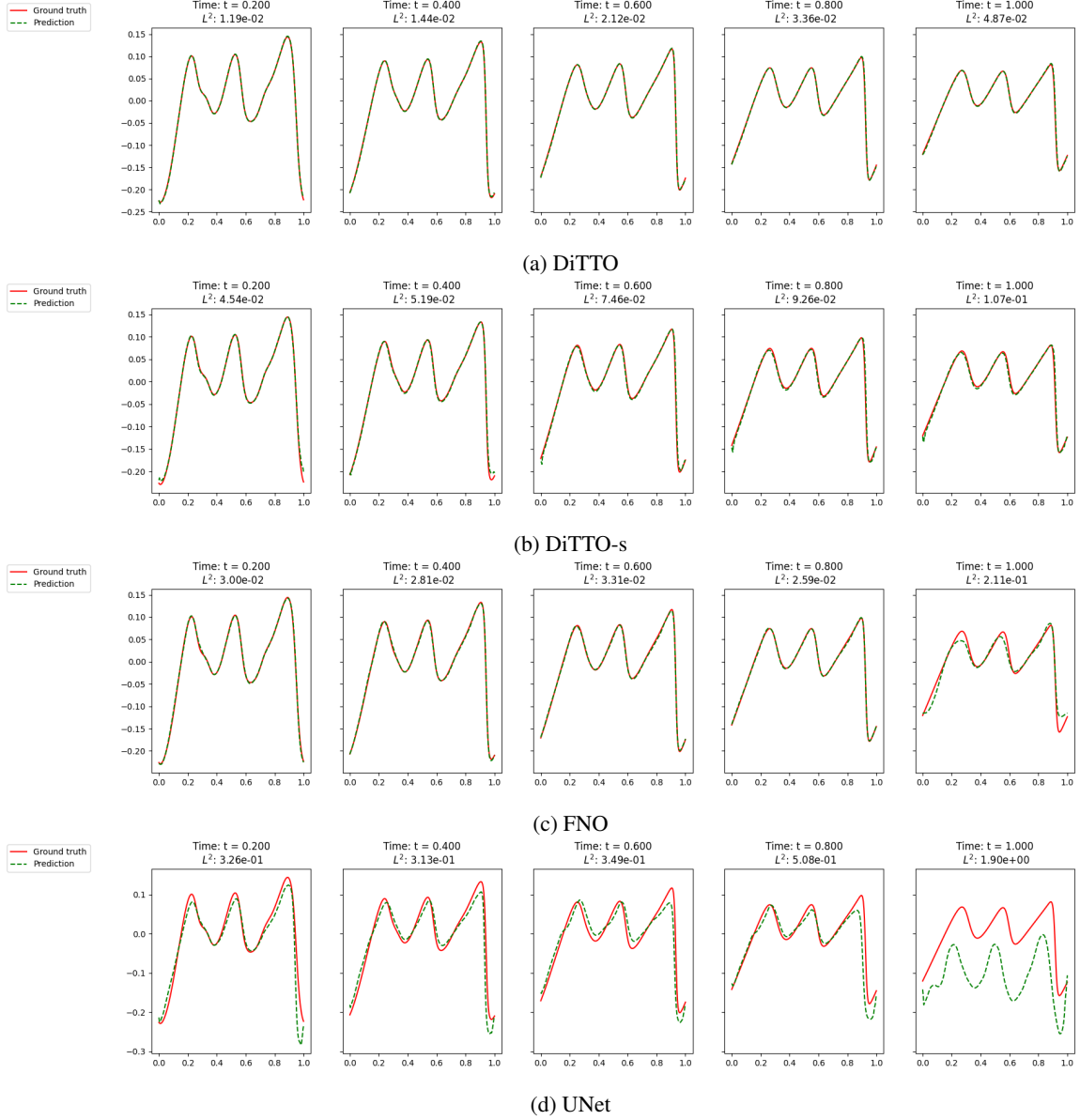
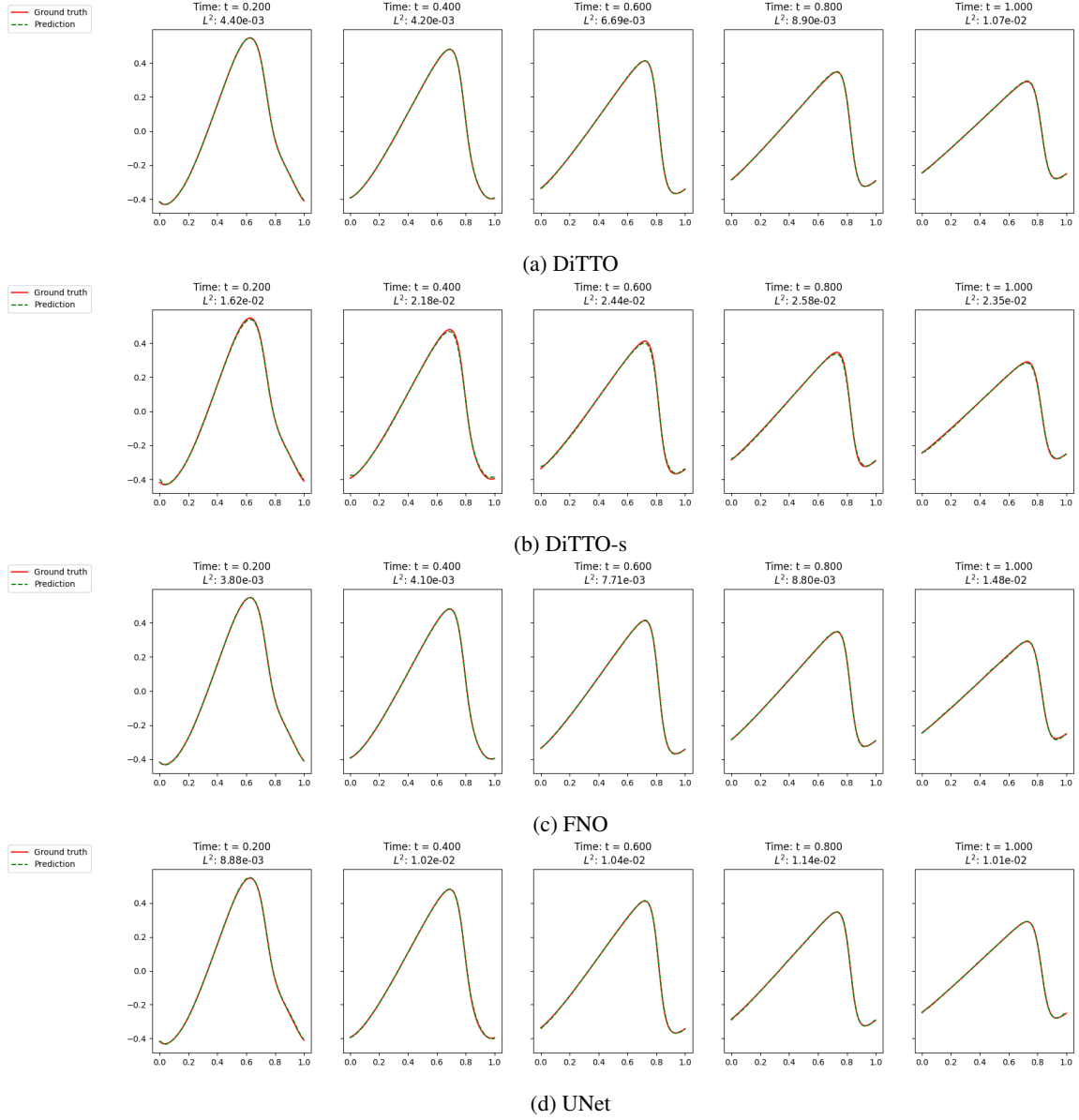


Figure 8: Burgers' scenario as described in Section 4.1 with $t_{final} = 1$, $\nu = 0.001$, $N_x = 256$ $N_t^{train} = 50$, and $N_t^{test} = 200$.

A.2 Results without zero-shot super-resolution in time

All figures presented in the main body of the paper pertain to $N_t^{test} = 200$ and $N_t^{train} = 50$, which is the more difficult case since it involves interpolation in time. Here we add figures for the case where $N_t^{test} = N_t^{train} = 50$, i.e., all models were tested on the same temporal resolution used in training.

We present these results to show that all models performed well in this scenario.


 Figure 9: Burgers' scenario 4.1 with $t_{final} = 1$, $\nu = 0.01$, $N_x = 128$, and $N_t^{test} = N_t^{train} = 50$.

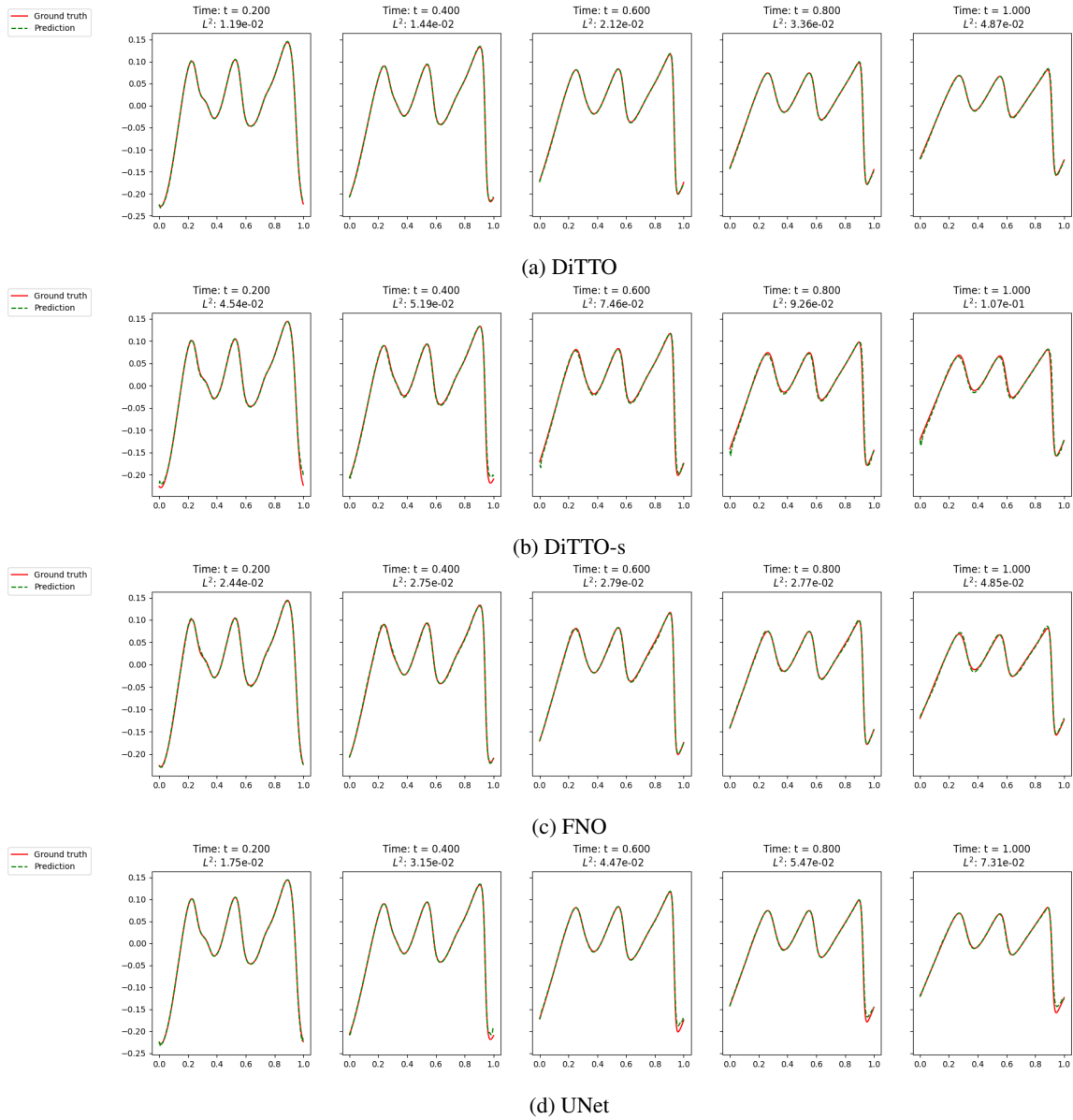


Figure 10: Burgers' scenario 4.1 with $t_{final} = 1$, $\nu = 0.001$, $N_x = 256$, and $N_t^{test} = N_t^{train} = 50$.

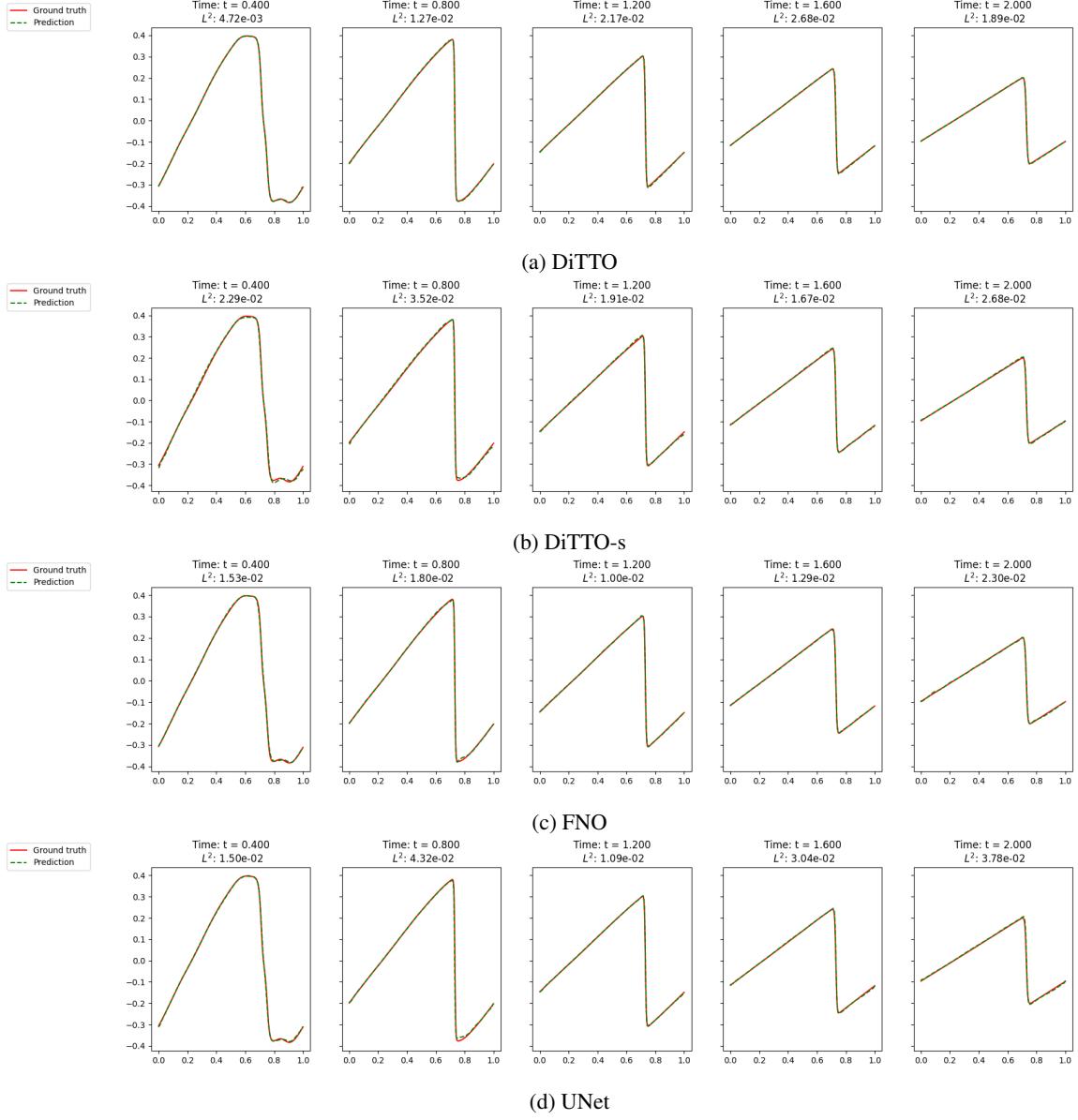


Figure 11: Burgers' scenario 4.1 with $t_{final} = 2$, $\nu = 0.001$, $N_x = 256$, and $N_t^{test} = N_t^{train} = 50$.

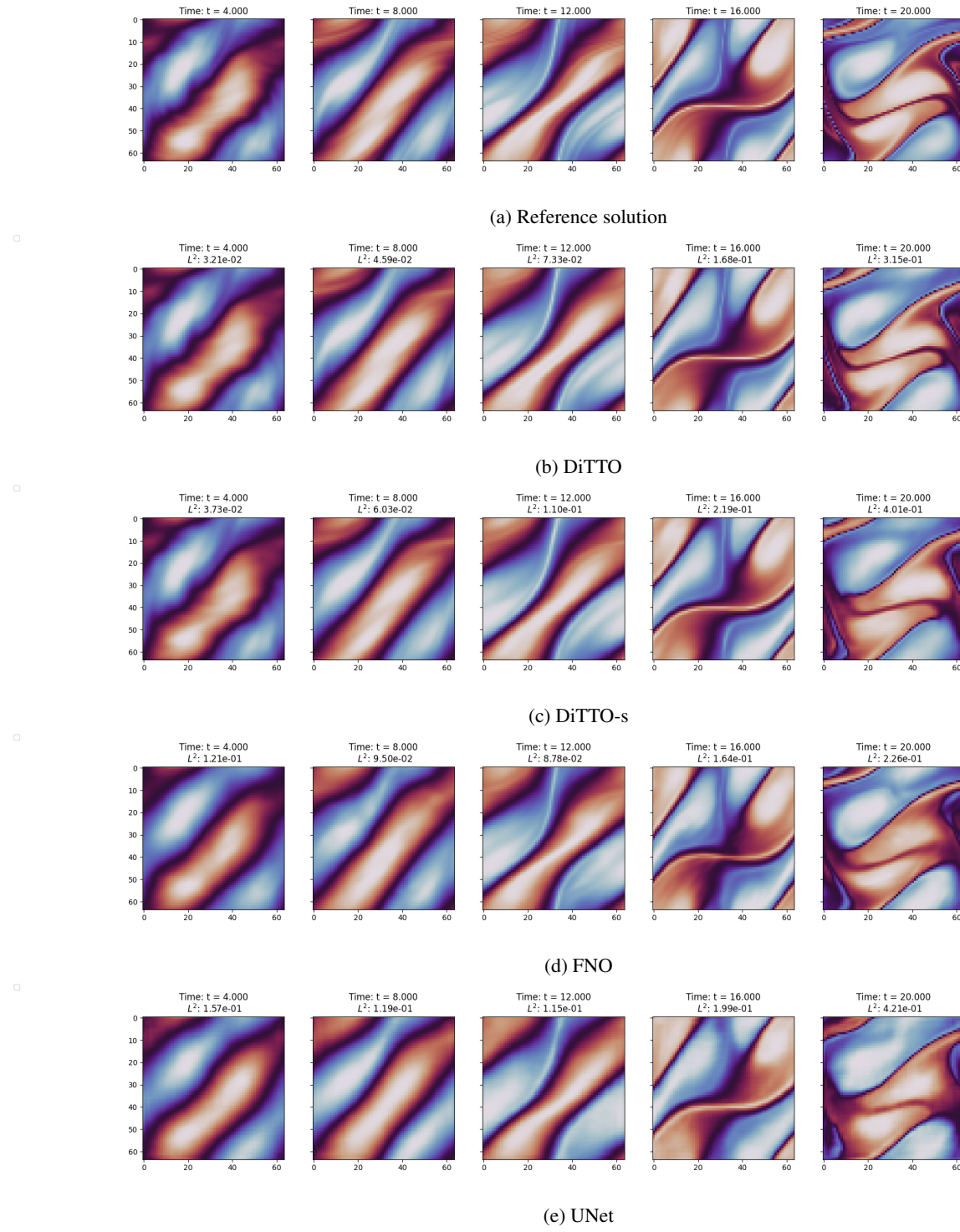


Figure 12: Navier-Stokes equations 4.2 with $Re \approx 2,000$ and $N_t^{test} = N_t^{train} = 50$.

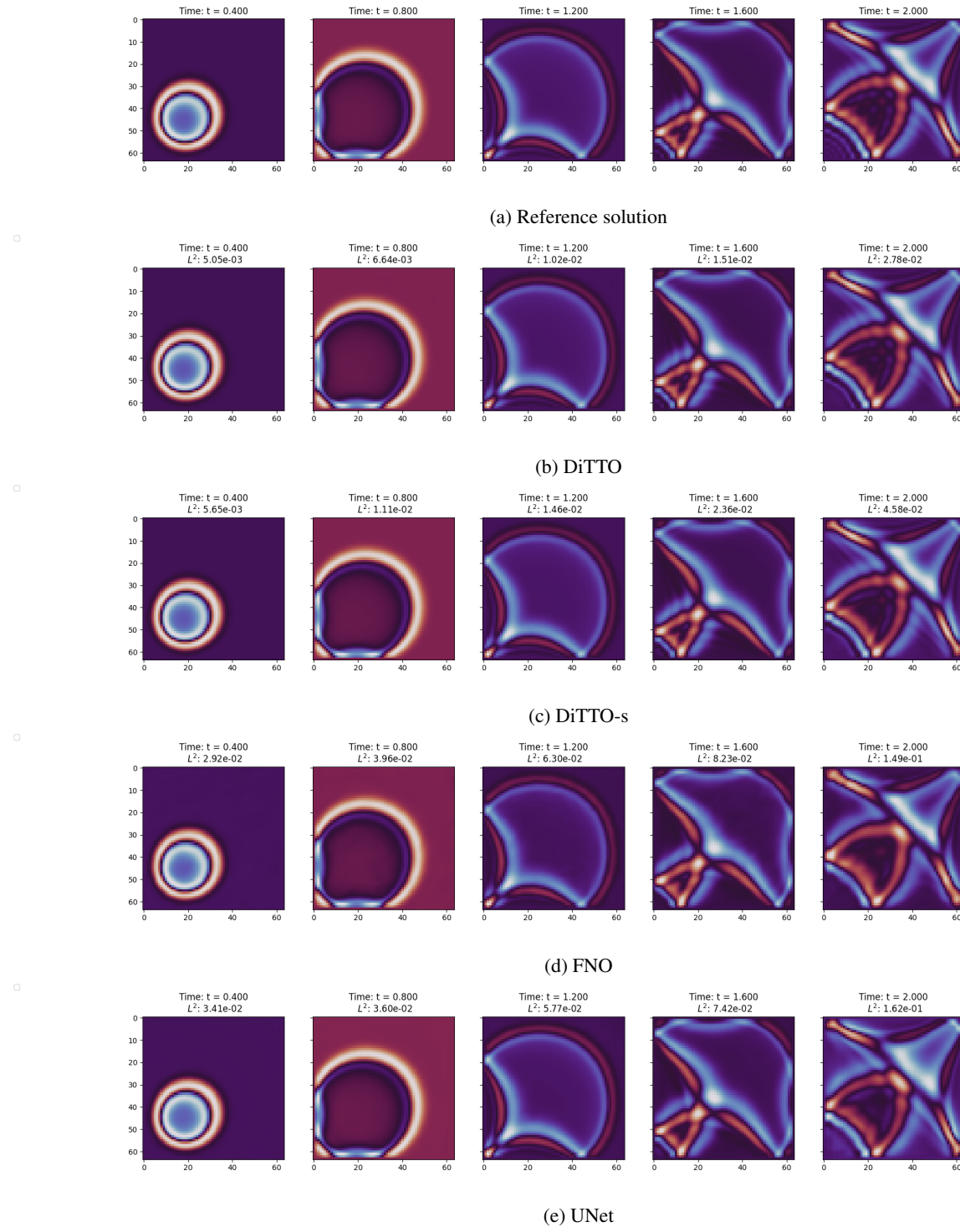


Figure 13: 2D Acoustic wave equation 4.3 with $N_t^{test} = N_t^{train} = 50$.

A.3 Ablation study

Here we present an ablation study related to the results shown in Section 4. Due to the computational cost of many experiments, we conducted the ablation study on one fixed scenario. Specifically, we used the Burgers’ dataset described in Section 4.1 with $\nu = 0.01$, $T = 1$, $N_x = 128$, and $N_t^{train} = 50$.

Influence of attention We examined the impact of the attention mechanism. To assess its contribution, we trained two models and compared them. The first model was DiTTO, as described in Section 3.3. The second model was the same, except we removed all attention layers. The full results are shown in Table 8. It is clear that the attention mechanism roughly halved the error values across all choices of N_t .

	$N_t^{test} = 10$	$N_t^{test} = 20$	$N_t^{test} = 50$	$N_t^{test} = 100$	$N_t^{test} = 200$
DiTTO	0.0060	0.0059	0.0058	0.0065	0.0070
DiTTO (no attention)	0.0132	0.0128	0.0126	0.0127	0.0128

Table 8: Relative L^2 test set errors with and without the attention mechanism for the Burgers’ scenario in Section 4.1 with $t_{final} = 1$, $\nu = 0.01$, $N_x = 128$, $N_t^{train} = 50$.

Effect of subsampling rate We experiment with different values of α as described in Section 3.5 and train several DiTTO-s models with corresponding subsampling rates. The results for $\alpha \in \{0.05, 0.1, 0.2, 1\}$ are shown in Table 9. We see that using the full data in each batch (i.e., $\alpha = 1$) does not necessarily produce the best results. Choosing $\alpha = 0.1$ and $\alpha = 0.2$ produced lower errors compared to $\alpha = 1$. However, $\alpha = 0.05$ was too small and consequently increased the error. Hence, choosing $\alpha = 0.1$ both improved the results and effectively reduced the batch size by 90%, and thus reduced the memory footprint of the model.

α	$N_t^{test} = 10$	$N_t^{test} = 20$	$N_t^{test} = 50$	$N_t^{test} = 100$	$N_t^{test} = 200$
1	0.0060	0.0059	0.0058	0.0065	0.0070
0.2	0.0058	0.0056	0.0056	0.0061	0.0066
0.1	0.0057	0.0056	0.0055	0.0061	0.0066
0.05	0.0250	0.0247	0.0247	0.0248	0.0248

Table 9: Relative L^2 test set errors using different subsampling rates α for the Burgers’ scenario in Section 4.1 with $t_{final} = 1$, $\nu = 0.01$, $N_x = 128$, $N_t^{train} = 50$.

FNO grid search To increase the validity of the comparison with FNOs, we conducted a hyperparameter search over various FNO architectures. We focused on the number of modes and the depth of the network, as defined in [3]. We tested for $N_t^{test} \geq 50$ to avoid padding issues for higher numbers of Fourier modes. The results are presented in Table 10. While wider, deeper FNO models generally obtained better results for $N_t^{test} = N_t^{train}$, we found that 4 layers with 18 Fourier modes gave the best results in the zero-shot super-resolution case. We followed a similar process for FNO-3D and decided to use 4 layers with 12 Fourier modes for the two-dimensional time-dependent problems.

# Fourier modes	# Layers	$N_t^{test} = 50$	$N_t^{test} = 100$	$N_t^{test} = 200$
12	4	0.0078	0.0112	0.0131
18	4	0.0048	0.0080	0.0100
24	4	0.0046	0.0146	0.0184
30	4	0.0041	0.0262	0.0312
12	8	0.0067	0.0087	0.0104
18	8	0.0052	0.0205	0.0274
24	8	0.0046	0.0162	0.0217
30	8	0.0041	0.0250	0.0292

Table 10: Relative L^2 test set errors using different FNO hyperparameter choices for the Burgers’ scenario in Section 4.1 with $t_{final} = 1$, $\nu = 0.01$, $N_x = 128$, $N_t^{train} = 50$.

A.4 FNO verification via super-resolution in space

Section 4 shows that the proposed DiTTO significantly outperforms FNOs in temporal super-resolution problems. In the original FNO paper [3], Li et al. present numerical examples in which FNO errors are independent of the size of the spatial grid. We use this attribute to verify the results of the trained FNOs compared to DiTTO. We test all FNO models on the Burgers' datasets 4.1 using spatial grid sizes that did not appear in the training set.

The results for all Burgers' scenarios are shown in Table 11. These results show that the FNO models are indeed grid-independent in space but less so in time.

Scenario	N_x	$N_t^{test} = 10$	$N_t^{test} = 20$	$N_t^{test} = 50$	$N_t^{test} = 100$	$N_t^{test} = 200$
$\nu = 0.01, T = 1$	128	0.1672	0.0217	0.0059	0.0100	0.0124
	256	0.1598	0.0274	0.0193	0.0201	0.0211
	512	0.1598	0.0275	0.0195	0.0204	0.0214
	1024	0.1598	0.0276	0.0197	0.0206	0.0215
$\nu = 0.001, T = 1$	128	0.2896	0.0463	0.0223	0.0266	0.0299
	256	0.2899	0.0461	0.0222	0.0265	0.0299
	512	0.2900	0.0461	0.0222	0.0265	0.0299
	1024	0.2901	0.0460	0.0221	0.0265	0.0299
$\nu = 0.001, T = 2$	128	0.3498	0.0581	0.0247	0.0315	0.0366
	256	0.3501	0.0582	0.0248	0.0315	0.0367
	512	0.3502	0.0583	0.0248	0.0315	0.0367
	1024	0.3502	0.0583	0.0248	0.0315	0.0367

Table 11: Test relative L^2 errors for the Burgers' equation 4.1 trained with $N_t^{train} = 50$.